

# Update of $\mathcal{H}\Phi$ : Newly added functions and methods in versions 2 and 3

Kota Ido<sup>a,\*</sup>, Mitsuaki Kawamura<sup>b</sup>, Yuichi Motoyama<sup>a</sup>, Kazuyoshi Yoshimi<sup>a</sup>, Youhei Yamaji<sup>c</sup>, Syngye Todo<sup>d,e,a</sup>, Naoki Kawashima<sup>a</sup>, Takahiro Misawa<sup>f,a,\*</sup>

<sup>a</sup>*Institute for Solid State Physics, The University of Tokyo, 5-1-5 Kashiwanoha, Kashiwa, Chiba 277-8581, Japan*

<sup>b</sup>*Information Technology Center, The University of Tokyo, Tokyo 113-8658, Japan*

<sup>c</sup>*Research Center for Materials Nanoarchitectonics, National Institute for Materials Science, Namiki, Tsukuba-shi, Ibaraki 305-0044, Japan*

<sup>d</sup>*Department of Physics, The University of Tokyo, Tokyo 113-0033, Japan*

<sup>e</sup>*Institute for Physics of Intelligence, The University of Tokyo, Tokyo 113-0033, Japan*

<sup>f</sup>*Beijing Academy of Quantum Information Sciences, Haidian District, Beijing 100193, China*

---

## Abstract

$\mathcal{H}\Phi$  [*aitch-phi*] is an open-source software package of numerically exact and stochastic calculations for a wide range of quantum many-body systems. In this paper, we present the newly added functions and the implemented methods in vers. 2 and 3. In ver. 2, we implement spectrum calculations by the shifted Krylov method, and low-energy excited state calculations by the locally optimal blocking preconditioned conjugate gradient (LOBPCG) method. In ver. 3, we implement the full diagonalization method using ScaLAPACK and GPGPU computing via MAGMA. We also implement a real-time evolution method and the canonical thermal pure quantum (cTPQ) state method for finite-temperature calculations. The Wannier90 format for specifying the Hamiltonians is also implemented. Using the Wannier90 format, it is possible to perform the calculations for the *ab initio* low-energy effective Hamiltonians of solids obtained by the open-source software RESPACK. We also update Standard mode—simplified input format in  $\mathcal{H}\Phi$ —to use these functions and methods. We explain the basics of the implemented methods and how to use them.

**Keywords:** Quantum lattice models; Exact diagonalization; Thermal pure quantum states; Real-time evolution; Excited spectrum.

---

## PROGRAM SUMMARY/NEW VERSION PROGRAM SUMMARY

*Program Title:*  $\mathcal{H}\Phi$  [*aitch-phi*]

*CPC Library link to program files:* (to be added by Technical Editor)

*Developer's repository link:* <https://github.com/issp-center-dev/HPhi>

*Code Ocean capsule:* (to be added by Technical Editor)

*Licensing provisions:* GPLv3

*Programming language:* C, Fortran

*Supplementary material:*

*Journal reference of previous version:*  
<https://www.sciencedirect.com/science/article/pii/S0010465517301200>

*Does the new version supersede the previous version?:* Yes. The latest version has compatibility with the old versions. Although most functions are available in newer versions, some redundant/unnecessary functions were abolished in newer versions.

*Reasons for the new version:* Implementation of new functions and methods, development of utilities, and bug fixes.

*Summary of revisions:* We added new functions to obtain excited spectrum, low-energy excited states, and time-dependent physical quantities. We also implemented the full diagonalization method by using MAGMA on GPGPUs and finite-temperature simulations by using the canonical thermal pure quantum state method. In addition, we developed utilities for connection with RESPACK and a submodule for a generator of input files.

*Nature of problem (approx. 50-250 words):* Physical properties in quantum lattice models with finite system sizes

*Solution method (approx. 50-250 words):* In  $\mathcal{H}\Phi$ , we implemented several numerical methods such as the Lanczos method, the full diagonalization method, the locally optimal block preconditioned conjugate gradient (LOBPCG) method, the real-time evolution method based on the Taylor expansion, the shifted Krylov method, and the microcanonical/canonical thermal pure quantum state method.

---

\*Corresponding authors.

*E-mail address:* ido@issp.u-tokyo.ac.jp

*E-mail address:* tmisawa@issp.u-tokyo.ac.jp

## 1. Introduction

To analyze properties of a quantum many-body system, eigenvalues and eigenvectors of the matrix representations of the Hamiltonians are crucially important. The exact diagonalization method <sup>1</sup> is one of the most basic tools for numerically obtaining the eigenvalues and eigenvectors of the Hamiltonians without any approximations [1]. Since the dimensions of the matrices increase exponentially as a function of number of sites  $N_s$  (for spin-1/2 systems, the number of dimensions is given by  $2^{N_s}$ ), the largest system size handled by the exact diagonalization method is significantly smaller than that of other numerical approaches and severely limited by the available memory size. Nevertheless, numerically exact results for small-size clusters are useful for examining the emergence of exotic quantum phases such as quantum spin liquids [2–4]. The numerically exact results are also useful for ensuring the accuracy of newly developed methods.

Numerical libraries for the diagonalization of the matrices such as LAPACK/ScaLAPACK [5, 6] have been developed and widely used. These libraries support the full and partial diagonalization of the given matrices stored in the memory, and the tractable matrix size for these libraries is on the order of  $10^5$  at most. For larger matrices, the power method (or more sophisticated Krylov subspace methods, such as the Lanczos method) is a widely used algorithm for obtaining the lowest eigenstate (ground state) or low-lying eigenstates (low-energy excited states). Since the power method and the Krylov subspace method mainly consist of matrix-vector products, namely, multiplications of Hamiltonian matrices by vectors <sup>2</sup>, the numerical costs and the required memory are largely reduced compared to full diagonalization. Using the Lanczos method, it becomes feasible in terms of cost to obtain the ground state of 36-site spin-1/2 systems, which has a dimensionality of  $2^{36} \sim 6.8 \times 10^{10}$ , for example. Moreover, it has been shown that numerically exact finite-temperature calculations are possible using a typical pure state [7–12], which can be generated by the power method. This method is often called the thermal pure quantum (TPQ) state method [9, 10] and can be applied to a wide range of quantum many-body systems.

In the field of condensed matter physics, several pioneering software packages in which the Lanczos

method is implemented have been developed, such as TITPACK [13] for spin-1/2 quantum spin systems, KOBEPACK [14] for spin-1 quantum spin systems, and SPINPACK [15] for both quantum spin systems and itinerant electron systems. In the ALPS project [16–18], the exact diagonalization method for a wide range of the quantum many-body systems is also implemented. These software packages have widely been used for analyzing ground states of the quantum many-body systems. However, inter-process distributed-memory parallelization is not supported in these software packages. Since the number of available cores rapidly increases in modern supercomputers, the implementation of the hybrid parallelization, i.e., combination of intra- and inter-node process parallelization, is necessary for efficient calculations.

Under those circumstances we developed and released  $\mathcal{H}\Phi$  ver.1.0 in 2016 [19, 20], which supports the hybrid parallelization combining OpenMP (intra-process shared-memory) and MPI (inter-process distributed-memory) parallelization. In  $\mathcal{H}\Phi$  ver.1.0, we implemented the Lanczos method for obtaining the ground states, the TPQ state method for finite-temperature calculations, and the full diagonalization using the LAPACK library.  $\mathcal{H}\Phi$  has been used to analyze a wide range of quantum many-body systems, such as quantum spin liquids [21–41], high- $T_c$  superconductors [42–44], and correlated topological phases [45, 46].  $\mathcal{H}\Phi$  is also used to examine the accuracy of developed numerical/theoretical methods [47–54].

After the release of  $\mathcal{H}\Phi$  ver.1.0, we continued to extend the applicable range of  $\mathcal{H}\Phi$  by implementing several functions and methods. Here, we summarize the most important functions and methods among the new additions in chronological order:

- Functions implementing spectrum calculation using the shifted Krylov method and the continued-fraction expansion method [55, 56] [**ver. 2.0.0**]
- Function implementing the locally optimal block preconditioned conjugate gradient (LOBPCG) method [57] for low-energy excited state calculations [**ver. 2.0.0**]
- Function implementing real-time evolution [**ver. 3.0.0**]
- Function implementing full diagonalization using ScaLAPACK [6] [**ver. 3.1.0**]
- Function implementing full diagonalization using GPGPU via MAGMA [58] [**ver. 3.1.0**]

<sup>1</sup>As we state below, we use the term “exact diagonalization” not only for the full diagonalization of a given matrix, but also for the partial diagonalization for obtaining a limited set of the eigenvalues and the eigenvectors.

<sup>2</sup>We often call vectors wave functions.

- Interface to RESPACK [59, 60], which derives *ab initio* effective Hamiltonians of solids [ver. 3.3.0]
- Making *Standard mode* submodule (Standard mode will be explained in Section 4) [ver. 3.4.0]
- Functions implementing the canonical TPQ (cTPQ) method [10] [ver. 3.5.0]

In the following sections of the present paper, we explain the basics of these functions and how to use them. We also show several examples of the implemented methods. Note that we do not explain the basic usage of  $\mathcal{H}\Phi$  and the methods/functions implemented in  $\mathcal{H}\Phi$  ver. 1 in this paper since they are already explained in Ref. [19]. In this paper, we mainly explain the above newly added functions and methods. For the basic usage of  $\mathcal{H}\Phi$ , please see the manual [61] as well as the tutorials [62].

The present paper is organized as follows: In Section 2, we explain how to install  $\mathcal{H}\Phi$  and the submodule repository of Standard mode. In Section 3.1, we explain full diagonalization with ScaLAPACK [6] on multiple CPUs and with MAGMA on multiple GPGPUs [58]. We also explain how to output matrices generated by the  $\mathcal{H}\Phi$  routines and how to input matrices prepared by the users in the Matrix Market exchange format for general sparse matrices. In Section 3.2, we explain spectrum calculation using  $\mathcal{H}\Phi$ . In  $\mathcal{H}\Phi$ , in addition to the conventional continued-fraction expansion method [1], the shifted-Krylov method [56, 63] is implemented. In Section 3.3, we detail the LOBPCG method [57, 64], which enables us to obtain several low-energy excited states simultaneously. We also show the effects of the preconditioning in the LOBPCG method. In Section 3.4, we explain how to perform real-time evolution using  $\mathcal{H}\Phi$ . In Section 3.5, we review the basics of the TPQ method. We also show that the cTPQ method indeed reproduces the results of the full diagonalization for the one-dimensional Heisenberg chain. In Section 4, we summarize the methods, models, and lattices available in Standard mode. In Section 5, we give an explanation of the interface to the Wannier90 format [65, 66] of the Hamiltonians. In Section 6, we explain the connection between  $\mathcal{H}\Phi$  and RESPACK [59, 60], which derives the *ab initio* low-energy effective Hamiltonians for solids from the outputs of the plane-wave density functional theory codes. Finally, Section 7 is devoted to the summary and future development of  $\mathcal{H}\Phi$ .

## 2. Installation

Before explaining the newly added functions, we explain how to download and install  $\mathcal{H}\Phi$ . We also explain the submodule repository of Standard mode.

### 2.1. How to download and install $\mathcal{H}\Phi$

$\mathcal{H}\Phi$  can be downloaded through the following GitHub repository:

```
https://github.com/issp-center-dev/HPhi
```

The latest version of  $\mathcal{H}\Phi$  is ver. 3.5.1. One can check the history and brief summaries of the releases on the release page [67]. On this page, one can download the gzipped tar files for each version, which contain source codes and manuals.

After ver. 3.0.0, we ended support for HPhiconfig.sh, which generates Makefiles. In the current version, to build  $\mathcal{H}\Phi$ , it is necessary to use the CMake utility [68] as follows:

```
$ cmake -B build -DConfig=$Config
$ cmake --build build
```

Typical examples of \$Config are given as follows:

- gcc : GCC
- intel: intel compiler + MKL library

To check whether  $\mathcal{H}\Phi$  has been installed correctly, we add several tests for CTest utility. One can run Ctest utility in the build directory by the following command.

```
$ cmake --build build --target test
```

To use ScaLAPACK for full diagonalization, it is necessary to specify the cmake option as

```
cmake -DUSE_SCALAPACK=ON
```

As we will explain in the next section,  $\mathcal{H}\Phi$  also supports full diagonalization by GPGPU via MAGMA. To use this function, it is necessary to install MAGMA. For detailed information on MAGMA including how to install it, one can refer to the official web page [69].

### 2.2. Submodule repository of Standard mode

In Standard mode of  $\mathcal{H}\Phi$ , one can conduct the calculations for predefined systems by preparing one simple and human-readable input file. Using Standard mode, the users can also generate all the necessary input files for Expert mode from one input file for Standard mode. For details of Standard and Expert modes, please refer to Ref. [19] and the manual [61]. Standard mode is also

used in mVMC [70, 71], which is a software package for the many-variable variational Monte Carlo method [72]. These two packages share the main part of Standard mode. Therefore, to make the maintenance of Standard mode easier, we separate Standard mode as a submodule in the independent repository at

<https://github.com/issp-center-dev/StdFace>

By using the following command, users can use the updated Standard mode in both  $\mathcal{H}\Phi$  and mVMC:

```
$ git submodule update -r -i
```

### 3. Newly added methods/functions

#### 3.1. Full diagonalization using GPGPU and ScaLAPACK

In  $\mathcal{H}\Phi$  ver. 1.0, full diagonalization was only implemented by calling `zheev` routine in LAPACK, which only supports the OpenMP parallelization in a single CPU processor. In  $\mathcal{H}\Phi$  ver. 3.1.0, we implement full diagonalization by ScaLAPACK, which enables us to perform full diagonalization by inter-process distributed-memory parallelization. It is necessary to specify the keyword `Scalapack` as “`Scalapack=1`” in the input file for Standard mode, or add a line “`Scalapack 1`” in `calcm0d.def` for *Expert mode* (Details of Expert mode are explained in Ref. [19]). Only by either one of these two minor modifications to the input file, one can perform full diagonalization by calling ScaLAPACK routine. The cost of the full diagonalization for matrices of  $O(10^5)$  linear dimensions becomes reasonable/cheap by ScaLAPACK.

We also implement full diagonalization on GPGPUs by calling a MAGMA routine `magma_zheevd` [58]. If MAGMA is installed on the user’s environment, by specifying the number of GPGPUs (e.g., `NGPU=2` in the input file of Standard mode or `NGPU 2` in `calcm0d.def` for Expert mode), one can perform full diagonalization on multi-GPGPU environments.

##### 3.1.1. Performance of the full diagonalization

To benchmark the different full diagonalization methods, we performed full diagonalization for the one-dimensional Heisenberg model. An example of the input file is given as follows:

```
L          = 12
model     = "SpinGC"
lattice   = "chain"
method    = "FullDiag"
J         = 1.0
```

By changing the system size  $L$ , the dimensions of the target matrices  $d_H = 2^L$  are increased. In Fig. 1, we show the elapsed time of the full diagonalization as a function of  $d_H$  for  $L = 8-14$ . For  $d_H \geq 2500$ , the full diagonalization by a single GPGPU is faster than that by a single CPU with 16 cores. For  $d_H = 2^{14} = 16384$ , the full diagonalization on GPGPU by the MAGMA routine is about ten times faster. We also find that the full diagonalization on a single GPGPU by MAGMA is still faster than that by ScaLAPACK using 16 nodes ( $2048 = 128 \times 16$  cores). This result demonstrates that GPGPU computing is an efficient tool for performing full diagonalization of matrices whose dimensions are around  $d_H \sim 10^4$ .

We note that the elapsed time summarized in Fig. 1 does not include that for calculations of physical quantities. If the full diagonalization method has been performed by using Standard mode, the elapsed time for calculations of physical quantities will be significantly longer than that of the full diagonalization of the Hamiltonian matrix. When we specify `OneBodyG` and `TwoBodyG` in `namelist.def`, correlation functions or static Green’s functions defined in `OneBodyG` and/or `TwoBodyG` are calculated for all the eigenstates. In these calculations on multi-process parallel environments, the eigenvectors in each MPI process are gathered into a single process and then the correlation functions are calculated in that process. This communication process becomes the most time-consuming part of the whole simulation when we use ScaLAPACK with a large number of MPI processes. For example, compared with the elapsed time of the full diagonalization by ScaLAPACK with 128 MPI processes summarized in Fig. 1, it takes about ten times longer to calculate the correlation functions generated by Standard mode.

##### 3.1.2. Output/Input by Matrix Market exchange format

In  $\mathcal{H}\Phi$ , it is also possible to output the Hamiltonian matrices of the quantum many-body systems in the Matrix Market exchange format [73] by specifying the keyword `HamIO="out"` in Standard mode or `OutputHam=1` in `calcm0d.def` in Expert mode. Here, we show an example of the output file (`zvo_Ham.dat`) in the Matrix Market exchange format: A simple  $2 \times 2$  matrix,

$$\mathcal{H} = \begin{pmatrix} 1 & -i \\ i & -1 \end{pmatrix}, \quad (1)$$

is outputted as follows:

```
% 2by2
2 2 4
1 1 1.0 0.0
```

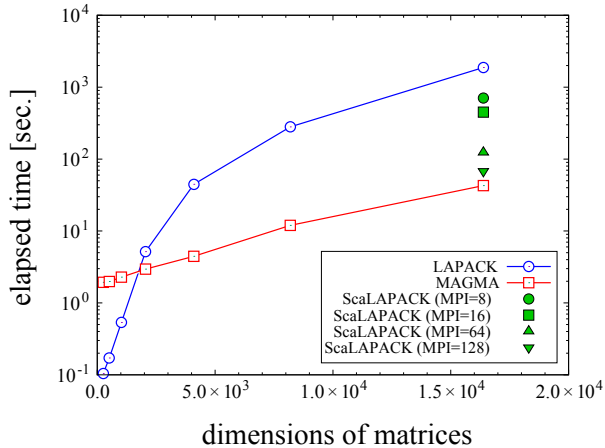


Figure 1: Comparison of elapsed time for full diagonalization for the one-dimensional antiferromagnetic Heisenberg chain by the `zheev` routine in LAPACK with 16 OpenMP threads, and the `magma_zheevd` routine with 16 OpenMP threads and a single GPGPU, NVIDIA HGX A100 40GB. The calculations are conducted at the supercomputer system C (kugui) at the ISSP Supercomputer Center, the University of Tokyo. The calculations are done for several system sizes, from  $L = 8$  (the matrix dimensions are  $2^8 = 256$ ) to  $L = 14$  (the matrix dimensions are  $2^{14} = 16384$ ). We also show the results obtained with ScaLAPACK with 16 OpenMP threads and  $L = 14$ . In ScaLAPACK, by increasing the number of the MPI processes, the elapsed time becomes shorter. However, full diagonalization on a single GPGPU is still faster than using ScaLAPACK with 128 MPI processes.

```
1 2 0.0 -1.0
2 1 0.0 1.0
2 2 -1.0 0.0
```

In the first line, we write the dimensions of the target matrix (the number of columns is 2 and the number of rows is 2) and the number of non-zero elements (in this case, 4). Other than the first line, the row (column) index,  $\ell$  ( $m$ ), and the real (imaginary) part of the matrix element,  $u$  ( $v$ ), are written in the order of

$$\ell \ m \ u \ v. \quad (2)$$

We note that indices of the row and column start from one (a start offset of one) as in the standard notation of Fortran. This function is useful for examining the structure of the matrices of quantum many-body systems. By specifying keywords in `modpara.def` and `calcm0d.def`, files in the Matrix Market exchange format can also be used as inputs for calculations of the full diagonalization method. The details are explained in  $\mathcal{H}\Phi$ 's manual [61].

### 3.2. Spectrum calculation

Using the eigenvectors,  $\mathcal{H}\Phi$  can calculate the dynamical correlation function, which is defined as

$$D(z) = \langle \Phi_{\text{ex}} | [zI - \hat{H}]^{-1} | \Phi_{\text{ex}} \rangle, \quad (3)$$

$$| \Phi_{\text{ex}} \rangle = \hat{O} | \Phi_0 \rangle, \quad (4)$$

where  $z$  is a given complex number,  $I$  is an identity matrix,  $\hat{H}$  is a Hamiltonian matrix,  $| \Phi_0 \rangle$  is the target eigenvector, and  $\hat{O}$  is the excitation operator. As excitation operators,  $\mathcal{H}\Phi$  implements single-particle excitations (`SingleExcitation`) and pair excitations (`PairExcitation`) defined as

$$\hat{O}_{\text{single}} = \begin{cases} \sum_{i,\sigma} A_{i\sigma} c_{i\sigma}^\dagger \\ \sum_{i,\sigma} A_{i\sigma} c_{i\sigma} \end{cases}, \quad (5)$$

$$\hat{O}_{\text{pair}} = \begin{cases} \sum_{i,j,\sigma,\tau} A_{i\sigma,j\tau} c_{i\sigma}^\dagger c_{j\tau} \\ \sum_{i,j,\sigma,\tau} A_{i\sigma,j\tau} c_{i\sigma} c_{j\tau}^\dagger \end{cases}, \quad (6)$$

where  $c_{i\sigma}^\dagger$  ( $c_{i\sigma}$ ) represents a creation (annihilation) operator in the second quantization, which generates (removes) a particle with  $\sigma$  spin at the  $i$ th site/orbital. We note that the users can specify the order of operators (order of the creation and annihilation operators) in the input file.

$\mathcal{H}\Phi$  implements two different algorithms for calculating the dynamical correlation function  $D(\omega)$ . One is the continued-fraction expansion based on the Lanczos method (`method="Lanczos"`) [1, 74] which is frequently used in previous studies. Another is the shifted Krylov-subspace method (`method="CG"`) [56, 63]. Since the details of the implementation of the shifted Krylov-subspace method are already given in Ref. [55], we just note the advantages of the shifted Krylov-subspace method in comparison with the conventional continued-fraction expansion. The advantages of the shifted Krylov-subspace method are summarized as follows:

1. We can explicitly evaluate the convergence of  $D(z)$ .
2. We can calculate the off-diagonal dynamical correlation functions, i.e.,  $D_{ab}(z) =$

$$\langle \Phi_0 | \hat{O}_a^\dagger [zI - \hat{H}]^{-1} \hat{O}_b | \Phi_0 \rangle.$$

On the first point, 2-norms of the residual vectors are output in `residual.dat`. The definition of the residual vector in the shifted Krylov subspace method is detailed in Ref. [55]. By examining `residual.dat`, one can quantify the accuracy of the convergence. On the second point, although  $\mathcal{H}\Phi$  does not support the function

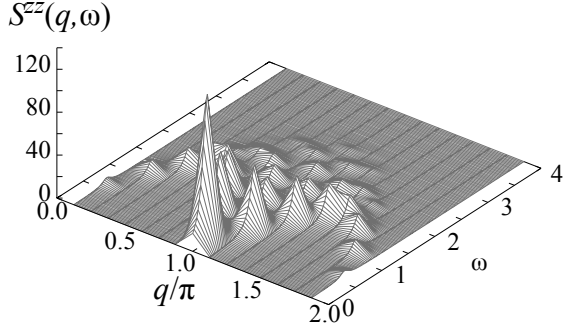


Figure 2: Dynamical spin structure factors for the one-dimensional antiferromagnetic Heisenberg chain. We take  $\eta = 0.1$ . We can see the signature of the des Cloizeaux-Pearson mode [76].

of computing off-diagonal dynamical correlation functions ( $a \neq b$ ), it is possible to calculate them by the shifted Krylov subspace method.

As an example of the dynamical correlation functions, we calculate the dynamical spin structure factors for the one-dimensional antiferromagnetic Heisenberg model defined as

$$S^{zz}(q, \omega) = -\text{Im} \left[ \langle \Phi_{\text{ex}}(q) | [(\omega + i\eta)I - \hat{H}]^{-1} | \Phi_{\text{ex}}(q) \rangle \right], \quad (7)$$

$$| \Phi_{\text{ex}} \rangle = \hat{O}_{\text{spin}} | \Phi_{\text{GS}} \rangle, \quad (8)$$

$$\hat{O}_{\text{spin}} = \sum_{\ell=0}^{L-1} \hat{S}_{\ell}^z e^{iq\ell} | \Phi_{\text{GS}} \rangle, \quad (9)$$

where  $| \Phi_{\text{GS}} \rangle$  is the ground state,  $\hat{S}_{\ell}^z = (c_{\ell\uparrow}^{\dagger} c_{\ell\uparrow} - c_{\ell\downarrow}^{\dagger} c_{\ell\downarrow})/2$ , and  $q [= 2\pi m/L (m \in \mathbb{Z})]$  represents the wave numbers. In Fig. 2, we show  $S^{zz}(q, \omega)$  for the  $L = 16$  Heisenberg chain obtained by the shifted Krylov method. The calculation flow chart is summarized as follows:

1. Calculating the ground state  $| \Phi_{\text{GS}} \rangle$
2. Preparing the `pair.def` that denotes  $\hat{O}_{\text{spin}} = \sum_{\ell} \hat{S}_{\ell}^z e^{iq\ell}$  for each  $q$
3. Calculating  $S^{zz}(q, \omega)$  using the shifted-Krylov method `method="CG"` in `calmod.def`

These three steps can be performed automatically by using a script `Spectrum.py` in Ref. [75]. By executing the following command, one can calculate  $S^{zz}(q, \omega)$  for the 16-site one-dimensional Heisenberg chain:

```
$ python3 Spectrum.py 16
```

```

Initialize  $| \Phi_n \rangle$  as normalized random vectors
 $| p_n \rangle := 0 \quad | H p_n \rangle := 0$ 
 $| H \Phi_n \rangle := \hat{H} | \Phi_n \rangle$ 
 $E_n := \langle \Phi_n | H \Phi_n \rangle$ 
loop iterations:
 $| r_n \rangle := | H \Phi_n \rangle - E_n | \Phi_n \rangle$ 
if all  $\sqrt{\langle r_n | r_n \rangle} < E_{\text{th}}$ : finish
if not first iteration:  $| r_n \rangle := \hat{T} | r_n \rangle$ 
 $| r_n \rangle := | r_n \rangle / \sqrt{\langle r_n | r_n \rangle}$ 
 $| H r_n \rangle := \hat{H} | r_n \rangle$ 
 $\hat{O}_{\text{sub}} := (\{ | r_n \rangle \}, \{ | \Phi_n \rangle \}, \{ | p_n \rangle \})^{\dagger} (\{ | r_n \rangle \}, \{ | \Phi_n \rangle \}, \{ | p_n \rangle \})$ 
 $\hat{H}_{\text{sub}} := (\{ | r_n \rangle \}, \{ | \Phi_n \rangle \}, \{ | p_n \rangle \})^{\dagger} (\{ | H r_n \rangle \}, \{ | H \Phi_n \rangle \}, \{ | H p_n \rangle \})$ 
Solve  $\hat{H}_{\text{sub}} \varphi_n = E_n^{\text{new}} \hat{O}_{\text{sub}} \varphi_n$ 
 $E_n := (E_n + E_n^{\text{new}})/2$ 
 $| \Phi_n \rangle := (\{ | r_m \rangle \}, \{ | \Phi_m \rangle \}, \{ | p_m \rangle \}) \cdot \varphi_n$ 
 $| H \Phi_n \rangle := (\{ | H r_m \rangle \}, \{ | H \Phi_m \rangle \}, \{ | H p_m \rangle \}) \cdot \varphi_n$ 
 $| p_n \rangle := (\{ | r_m \rangle \}, 0, \dots, 0, \{ | p_m \rangle \}) \cdot \varphi_n$ 
 $| H p_n \rangle := (\{ | H r_m \rangle \}, 0, \dots, 0, \{ | H p_m \rangle \}) \cdot \varphi_n$ 
 $| \Phi_n \rangle := | \Phi_n \rangle / \sqrt{\langle \Phi_n | \Phi_n \rangle}$ 
 $| H \Phi_n \rangle := | H \Phi_n \rangle / \sqrt{\langle \Phi_n | \Phi_n \rangle}$ 
 $| p_n \rangle := | p_n \rangle / \sqrt{\langle p_n | p_n \rangle}$ 
 $| H p_n \rangle := | H p_n \rangle / \sqrt{\langle p_n | p_n \rangle}$ 
end loop iterations

```

Figure 3: Algorithm of LOBPCG method. Here,  $n$  is the index of eigenstates and  $E_{\text{th}}$  is the energy threshold for the convergence criteria.  $\{\dots\}$  indicates a set whose size is the number of the target eigenstates.

### 3.3. Iterative diagonalization method for multiple eigenvectors

The locally optimal block preconditioned conjugate gradient (LOBPCG) method [57] is implemented in  $\mathcal{H}\Phi$ . Using the LOBPCG method, we can simultaneously obtain several low-energy excited states in one calculation. Since the orthogonality of each eigenvector is automatically guaranteed, we can also determine the degeneracy of the low-energy excited states. Although the Lanczos method can also be used to obtain the low-energy excited states, it needs additional treatment, such as the re-orthogonalization of the obtained eigenvectors. As we detail below, the procedure of the LOBPCG method is simple and straightforward.

Here, we briefly explain the algorithm of the LOBPCG method. In the LOBPCG method, in addition to the candidate vectors of the eigenstates  $\{ | \Phi_n \rangle \}$ , we calculate residual vectors  $\{ | r_n \rangle \}$ , conjugate gradient vectors  $\{ | p_n \rangle \}$ , and those to which the Hamiltonian is applied  $\{ | H \Phi_n \rangle \}$ ,  $\{ | H r_n \rangle \}$ ,  $\{ | H p_n \rangle \}$  ( $n = 0, \dots, M - 1$ , where  $M$  is the number of the target eigenstates). Using these vectors, we define the following Hamiltonian in

the subspace and the overlap matrix as

$$\hat{H}_{\text{sub}} = \langle V | \hat{H} | V \rangle, \quad (10)$$

$$\hat{O}_{\text{sub}} = \langle V | V \rangle, \quad (11)$$

$$|V\rangle = (\{|r_n\rangle\}, \{|\Phi_n\rangle\}, \{|p_n\rangle\}). \quad (12)$$

We note that the dimension of  $\hat{H}_{\text{sub}}$  is the number of target eigenstates times three, namely  $(3M)$ . We solve the following generalized eigenvalue equation for the subspace:

$$\hat{H}_{\text{sub}} \boldsymbol{\varphi}_n = E_n^{\text{new}} \hat{O}_{\text{sub}} \boldsymbol{\varphi}_n. \quad (13)$$

In the actual calculation, we solve the equation using LAPACK. By using obtained eigenvectors  $\boldsymbol{\varphi}_n$ , we update  $\{|\Phi_n\rangle\}, \{H\Phi_n\rangle\}, \{|p_n\rangle\}$ , and  $\{Hp_n\rangle\}$  as follows:

$$|\Phi_n\rangle = (\{|r_m\rangle\}, \{|\Phi_m\rangle\}, \{|p_m\rangle\}) \cdot \boldsymbol{\varphi}_n, \quad (14)$$

$$|H\Phi_n\rangle = (\{|Hr_m\rangle\}, \{H|\Phi_m\rangle\}, \{H|p_m\rangle\}) \cdot \boldsymbol{\varphi}_n, \quad (15)$$

$$|p_n\rangle = (\{|r_m\rangle\}, 0, \dots, 0, \{|p_m\rangle\}) \cdot \boldsymbol{\varphi}_n, \quad (16)$$

$$|Hp_n\rangle = (\{|Hr_m\rangle\}, 0, \dots, 0, \{Hp_m\rangle\}) \cdot \boldsymbol{\varphi}_n, \quad (17)$$

where we use the simplified notation

$$|\Phi_n\rangle = (\{|r_m\rangle\}, \{|\Phi_m\rangle\}, \{|p_m\rangle\}) \cdot \boldsymbol{\varphi}_n \quad (18)$$

$$= \sum_{m=0}^{M-1} [\varphi_{nm} |r_m\rangle + \varphi_{n,m+M} |\Phi_m\rangle + \varphi_{n,m+2M} |p_m\rangle]. \quad (19)$$

Here,  $\varphi_{nm}$  is the  $m$ th component of the  $n$ th eigenvector  $\boldsymbol{\varphi}_n$ . Finally, we normalize the updated vectors, for example,  $|\Phi_n\rangle \leftarrow |\Phi_n\rangle / |\Phi_n\rangle$ . By performing the procedure iteratively, we can shift the subspace to the lower energy manifold. Figure 3 summarizes the procedure of the LOBPCG method.

In each iteration, we multiply the residual vectors  $|r_n\rangle$  by the preconditioner  $\hat{T}$  to accelerate the convergence. It is known that the convergence becomes faster if the eigenvalues are distributed around 1 [77]. Therefore, the ideal preconditioner is given by  $\hat{T} = (\hat{H} - E_n)^{-1}$ , which makes the modified eigenvalues around the ground states located around 1 ( $\tilde{E}_0 = E_0/E_0 = 1, \tilde{E}_1 = E_1/E_0 \sim 1, \dots$ ). However, it is impossible to take  $\hat{T} = (\hat{H} - E_n)^{-1}$ . Thus, one of the main problems to be addressed in preconditioning is how to approximate  $(\hat{H} - E_n)^{-1}$ . By taking the approximate form of  $(\hat{H} - E_n)^{-1}$  appropriately, it is possible to accelerate the convergence [64].

In  $\mathcal{H}\Phi$ , following Ref. [64], we implement the adaptively shifted point Jacob method to approximate  $(\hat{H} - E_n)^{-1}$ . In this method, we only consider the diagonal elements of  $(\hat{H} - E_n)^{-1}$  and approximate them as

$$T_{pq} = \frac{\delta_{pq}}{H_{pp} - \tilde{E}_n}, \quad (20)$$

$$\begin{aligned} \tilde{E}_n &:= E_n - E_{\text{LB}} \\ \text{if } \sqrt{\langle r_n | r_n \rangle} < 1: \\ & \quad i_E := \text{int}(\log_{10} \tilde{E}_n) \\ & \quad i_r := \text{int}(\log_{10} \sqrt{\langle r_n | r_n \rangle}) + 1 \\ & \quad \tilde{E}_n := 10^{i_E + i_r} \text{int}(\tilde{E}_n / 10^{i_E + i_r}) \\ \text{else:} \\ & \quad \tilde{E}_n := 0 \\ \text{end if} \\ \tilde{E}_n &:= \tilde{E}_n + E_{\text{LB}} \\ T_{pq} &:= \delta_{pq} / (H_{pp} - \tilde{E}_n) \end{aligned}$$

Figure 4: Algorithm of the adaptively shifted point Jacob method.  $E_{\text{LB}}$  is a constant that is lower than the ground-state energy  $E_{\text{GS}}$  ( $E_{\text{LB}} < E_{\text{GS}}$ ).

where  $\tilde{E}_n$  is determined by the procedure shown in Fig. 4. Since we adaptively determine  $\tilde{E}_n$  to approach the true eigenvalue from below ( $E_{\text{LB}} \leq \tilde{E}_n < E_{\text{GS}}$ , where  $E_{\text{LB}}$  is an estimated lower-bound constant of the ground-state energy and  $E_{\text{GS}}$  is the true ground-state energy), the preconditioning increases the weights of eigenvectors around the ground states. This indicates that the preconditioning can efficiently extract the weights of the eigenvectors around the ground states. In contrast to this, if we use  $E_n$ , which is always larger than the true ground-state energy, the preconditioning increases the weights of eigenvectors other than the ground states. It is pointed out that the use of  $E_n$  sometimes causes unstable convergence [64].

The concrete procedure of the preconditioning is shown in Fig. 4. In the point Jacob method, since we just approximate  $\hat{T}$  as a diagonal matrix, we need no extra memory or computational cost. Nevertheless, as we show later, the convergence can be accelerated. In the actual calculations, the lower bound of the ground-state energy  $E_{\text{LB}}$  is estimated from the parameters of the second quantized Hamiltonian ( $t, J, U$ , and so on). We note that the Gershgorin circle theorem [78] is often used to estimate the lower bound of the ground-state energy. However, to use this theorem, it is necessary to evaluate all non-zero matrix elements and its numerical cost is large for large system sizes. Thus, we do not use the Gershgorin circle theorem but use a simple estimation of the lower bound from the parameters in the Hamiltonian.

Here, we examine the effects of the preconditioning. Figure 5 shows the convergence behavior of the LOBPCG method in the 16-site Hubbard model on the square lattice and the 30-site  $XXZ$  model on the kagome lattice. We vary the parameters  $U$  and  $J_z$  to see the pre-

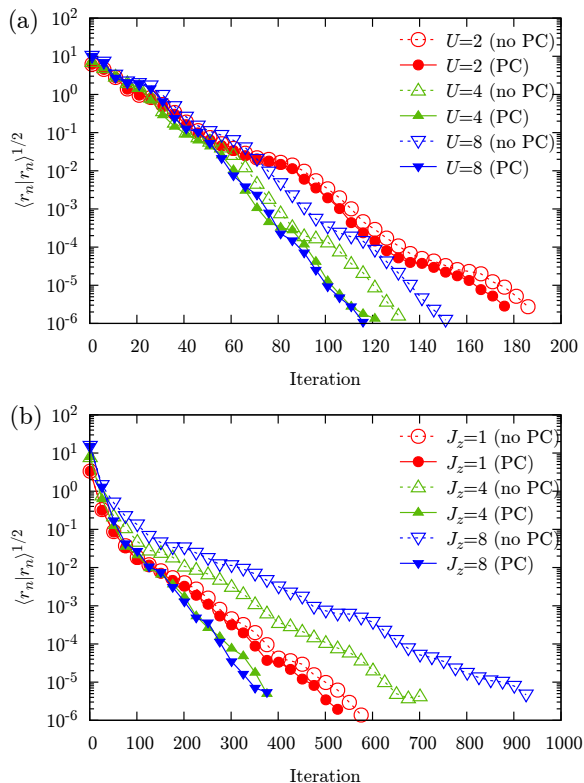


Figure 5: Convergence of the LOBPCG method for (a) the 16-site Hubbard model on the square lattice ( $t = -1$ ) and (b) the 30-site XXZ model on the kagome lattice ( $J_x = J_y = 1$ ). Dashed (solid) lines with empty (filled) symbols indicate the result without (with) preconditioning. Circles and upward and downward triangles in (a) [(b)] indicate the result of  $U = 2, 4$ , and  $8$  ( $J_z = 1, 4$ , and  $8$ ), respectively. In this calculation, we obtain 32 eigenstates simultaneously.

conditioning effects since these parameters affect the diagonal part of the Hamiltonian. In all cases, we can confirm that the preconditioning accelerates the convergence. We can also confirm that the convergence becomes faster for large  $U$  and large  $J_z$ . This is because the  $\hat{T}$  matrix becomes a good approximation of  $(\hat{H} - E_n)^{-1}$  for larger  $U$  or  $J_z$  since the absolute value of the diagonal part increases. For the standard Hamiltonians such as the Heisenberg model or the Hubbard model, we can confirm that the preconditioning is efficient. However, it is not clear how the preconditioning affects the convergence in general Hamiltonians. Therefore, in the current version of  $\mathcal{H}\Phi$ , preconditioning is switched off in the default settings, i.e.,  $\hat{T} = I$ . If users want to examine the effects of preconditioning, please add the following parameter in `modpara.def`.

PreCG 1

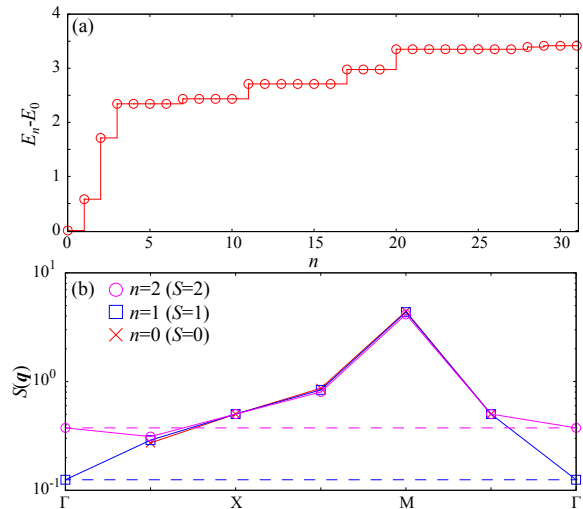


Figure 6: (a) Energies of 32 low-energy excited states measured from the ground-state energy  $E_0$  for  $4 \times 4$  antiferromagnetic Heisenberg model (total  $S_z = 0$  sector). (b) Spin structure factors for three low-energy excited states. The spin structure factors at  $\mathbf{q} = 0$  are given by  $S(\mathbf{q}) = S(S+1)/N_s$ , where  $S$  is the total spin. The horizontal broken lines show  $S(S+1)/N_s$  for  $S = 1$  and  $S = 2$ . The amplitude of  $S(\mathbf{0})$  for the ground state is less than  $10^{-8}$ .

We next show another example of an application of the LOBPCG method. By using the LOBPCG method, we obtain the low-energy excited states of the two-dimensional antiferromagnetic Heisenberg model ( $N_s = 4 \times 4$ , total  $S_z$  is zero). An input file is given as follows.

```
L           = 4
W           = 4
lattice    = "square"
model     = "Spin"
method    = "CG"
J          = 1
2Sz       = 0
exct      = 32
```

In Fig. 6, we show the eigenenergies obtained by the LOBPCG method. We simultaneously obtain 32 low-energy excited states. By calculating the spin structure factors, we can see that the triplet ( $S = 1$ ) [the quadruplet ( $S = 2$ )] state is the first [second] excited state. As is shown in this example, the LOBPCG method offers information on the quantum numbers and the degeneracies of the low-energy excited states, which are often used for identifying the nature of quantum magnets.

### 3.4. Real-time evolution

For a given wave function (not limited to an eigenstate), one can perform real-time evolution by solving



the following time-dependent Schrodinger equation:

$$i \frac{\partial |\Phi(t)\rangle}{\partial t} = \hat{H}(t) |\Phi(t)\rangle. \quad (21)$$

By discretizing time with the width  $\Delta t$ , we can obtain the solution of the Schrodinger equation as follows:

$$|\Phi(t + \Delta t)\rangle = \exp[-i\hat{H}\Delta t] |\Phi(t)\rangle, \quad (22)$$

$$\sim \sum_{n=0}^{n_{\max}} \frac{1}{n!} (-i\hat{H}\Delta t)^n |\Phi(t)\rangle. \quad (23)$$

This indicates that real-time evolution can be done by multiplying the Hamiltonians by the wave functions. The default values are set as  $n_{\max} = 10$  and  $\Delta t = 0.01$  from Standard mode ver. 0.5. The unit of the time  $t$  and the time grid  $\Delta t$  is the inverse of that of the energy. By checking  $\langle \Phi(t) | \Phi(t) \rangle = 1$ , one can examine the accuracy of the real-time evolution.

To perform real-time evolution, it is necessary to specify the method as

```
method = "Time-Evolution"
```

```
in calmode.def.
```

For real-time evolutions, we provide two modes, Expert mode and Standard mode, for specifying time-dependent Hamiltonians. In Expert mode, users can define time-dependent Hamiltonians with arbitrary one- and two-body terms represented as

$$\begin{aligned} \hat{H}(t) = & - \sum_{i,j} t_{ij}(t) c_{r_i\sigma_i}^\dagger c_{r_j\sigma_j} \\ & + \sum_{i,j,k,l} I_{ijkl}(t) c_{r_i\sigma_i}^\dagger c_{r_j\sigma_j} c_{r_k\sigma_k}^\dagger c_{r_l\sigma_l}, \end{aligned} \quad (24)$$

where  $c_{r\sigma}^\dagger$  and  $c_{r\sigma}$  denote respectively the creation and annihilation operators of a particle with spin  $\sigma$  ( $\sigma = \uparrow$  or  $\downarrow$ ) at site  $r$ . In Standard mode,  $\mathcal{H}\Phi$  can perform real-time simulations on typical nonequilibrium systems such as in quench dynamics and electron systems irradiated by a laser. For details on specifying the time-dependent Hamiltonians, see the manual of  $\mathcal{H}\Phi$  [61].

As an example of quantum dynamics using  $\mathcal{H}\Phi$ , we show sudden quench dynamics in the one-dimensional Hubbard model at half filling. The Hamiltonian is defined by the following equation:

$$\hat{H}_{\text{quench}}(t) = -t_{\text{hop}} \sum_{\langle i,j \rangle} \sum_{\sigma} c_{i\sigma}^\dagger c_{j\sigma} + U(t) \sum_i n_{i\uparrow} n_{i\downarrow},$$

where  $\langle i, j \rangle$  denotes the indices of the nearest neighbor sites  $i$  and  $j$  on the one-dimensional chain,  $N_s$  denotes

the system size, and

$$U(t) = \begin{cases} U_0 & (t < 0), \\ U_{\text{quench}} & (t \geq 0). \end{cases} \quad (25)$$

For the sudden quench simulation, the total energy  $\langle \mathcal{H}(t) \rangle$  should be conserved after the interaction quench because the interaction term  $U(t)$  defined in Eq. (25) does not have time-dependence for  $t \geq 0$ . In addition, the norm of the wave function  $\langle \Phi(t) | \Phi(t) \rangle$  should not change during any unitary dynamics in quantum systems. To check whether these properties are satisfied during  $\mathcal{H}\Phi$  simulation, the time-dependence of the norm and the total energy are outputted to Norm.dat and SS.dat in the output directory, respectively. Figure 7 shows the  $n_{\max}$  and  $\Delta t$  dependence of these quantities and the double occupancy,

$$d = \frac{1}{N_s} \sum_i \langle n_{i\uparrow} n_{i\downarrow} \rangle, \quad (26)$$

during a sudden quench. We see that the conservation laws of the norm and the energy are satisfied for sufficiently large  $n_{\max}$  and small time step. The dynamics of double occupancy also converge under such conditions. The double occupancy shows a damped oscillation, which is often observed in sudden quench systems [79, 80].

### 3.5. cTPQ

#### 3.5.1. Basics of the TPQ method

Here, we briefly summarize the basics of the TPQ states and the difference between the microcanonical TPQ (mTPQ) state [9] and the canonical TPQ (cTPQ) state [10]. We note that the two methods are equivalent if we take appropriate hyperparameters. In  $\mathcal{H}\Phi$ , both methods are implemented. As we detail below, because error estimation of the cTPQ method is straightforward compared with the mTPQ method, we recommend that users use the cTPQ method in actual calculations.

The TPQ state is defined in

$$|\Phi(\beta)\rangle = \exp\left[-\frac{\beta\hat{H}}{2}\right] |\Phi_{\text{rand}}\rangle, \quad (27)$$

$$|\Phi_{\text{rand}}\rangle = \sum_x a_x |x\rangle, \quad (28)$$

where  $\beta$  represents the inverse temperature and  $\{|x\rangle\}$  is a basis set that spans the Hilbert space. For example, for a Hamiltonian conserving the total particle number,  $x$  may be the set of coordinates of particles, and for a quantum spin Hamiltonian conserving the total  $S_z$ ,  $x$

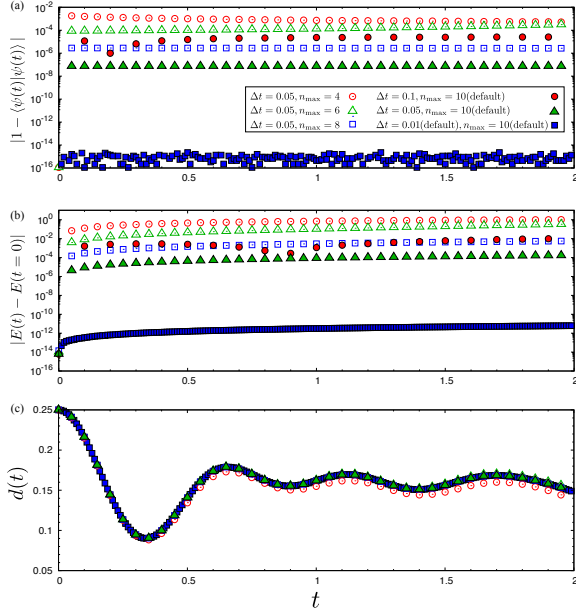


Figure 7: Time-dependence of (a) norms, (b) energies, and (c) double occupancies during the sudden quench dynamics in the one-dimensional Hubbard model for  $U_0/t_{\text{hop}} = 0$ ,  $U_{\text{quench}}/t_{\text{hop}} = 8$ , and  $N_s = 10$ . Legends of panels (b) and (c) are the same as those of panel (a). The units of the energy and the time are  $t_{\text{hop}}$  and  $t_{\text{hop}}^{-1}$ , respectively. In  $\mathcal{H}\Phi$ , the defaults of  $\Delta t$  and  $n_{\text{max}}$  are set to 0.01 and 10, respectively. To enhance the visibility of the energy difference during the real-time evolution, the energy at  $t = 0$  outputted in the simulation with the default parameters is used as  $E(t = 0)$ .

may be the set of spin positions in the real space. In the actual calculations, we take the random number  $a_x$  as uniformly distributed on the  $d_{\text{H}}$ -dimensional hypersphere, where  $d_{\text{H}}$  is the dimensionality of the Hilbert space of the given system. If we can assume the initial random vectors uniformly include all the eigenstates  $|n\rangle$ ,  $|\Phi_{\text{rand}}\rangle$  can be expressed as

$$|\Phi_{\text{rand}}\rangle = \sum_n a_n |n\rangle, \quad (29)$$

where the weight  $|a_n|$  can be approximated as  $1/d_{\text{H}}$ . Under this assumption, for example, the expectation value of a Hamiltonian is evaluated as

$$\langle \hat{H} \rangle = \frac{\langle \Phi(\beta) | \hat{H} | \Phi(\beta) \rangle}{\langle \Phi(\beta) | \Phi(\beta) \rangle} = \frac{\sum_n |a_n|^2 E_n e^{-\beta E_n}}{\sum_n |a_n|^2 e^{-\beta E_n}} \quad (30)$$

$$\sim \frac{\sum_n E_n e^{-\beta E_n}}{\sum_n e^{-\beta E_n}} = E(\beta). \quad (31)$$

This is the ensemble average of the energy. We note that this rough argument can be mathematically justified based on probability theory [12]. As shown in the

literature [10], the expectation values with respect to the TPQ state can reproduce by the ensemble average even the physical quantities that do not commute with the Hamiltonian. Therefore, the main task of the TPQ calculation is to generate  $|\Phi(\beta)\rangle$ , in other words, to numerically apply the exponential operator  $e^{-\beta \hat{H}/2}$  to the random initial vector  $|\Phi_{\text{rand}}\rangle$ .

According to Sugiura and Shimizu [9, 10], there are two ways to calculate  $|\Phi(\beta)\rangle$ : the microcanonical TPQ (mTPQ) state and the canonical TPQ (cTPQ) state. In the following, we give their definitions. We rewrite the TPQ state by using the imaginary time-evolution operator  $\hat{U}(\Delta\tau)$  as

$$\exp\left[-\frac{\beta}{2}\hat{H}\right]|\Phi_{\text{rand}}\rangle \sim \hat{U}(\Delta\tau)^k |\Phi_{\text{rand}}\rangle, \quad (32)$$

where  $\Delta\tau$  represents the slice width of the imaginary time evolution. In the cTPQ state, the definition of  $\hat{U}(\Delta\tau)$  is straightforward and given as

$$\exp\left[-\frac{\Delta\tau}{2}\hat{H}\right] \sim \sum_{n=0}^{n_{\text{max}}} \frac{1}{n!} \left(-\frac{\Delta\tau}{2}\hat{H}\right)^n \equiv \hat{U}_c(\Delta\tau) \quad (33)$$

$$|\Phi_{\text{cTPQ}}(\beta_k)\rangle = [\hat{U}_c(\Delta\tau)]^k |\Phi_{\text{rand}}\rangle, \quad (34)$$

$$\beta_k = k\Delta\tau. \quad (35)$$

In other words, we just expand  $\hat{U}(\Delta\tau)$  with respect to  $\Delta\tau$ . In the cTPQ calculation,  $n_{\text{max}}$  and  $\Delta\tau$  are hyperparameters. As we show later,  $n_{\text{max}} = 10$  and  $\Delta\tau = 0.01J$  give well-converged results in the one-dimensional antiferromagnetic Heisenberg model. In  $\mathcal{H}\Phi$ , we implement this Taylor expansion-based method of constructing the cTPQ method because of its simplicity and generality. We note that the cTPQ state can also be constructed from the mTPQ state as is shown in Ref. [10].

In contrast, the definition of  $\hat{U}(\Delta\tau)$  in the mTPQ state is rather elaborate. In the mTPQ state,  $\hat{U}(\Delta\tau)$  is defined as

$$\hat{U}_m(\Delta\tau) \equiv \left(1 - \frac{\Delta\tau}{2}\hat{H}\right), \quad \Delta\tau = \frac{2}{lN_s}, \quad (36)$$

$$|\Phi_{\text{mTPQ}}(\beta_k)\rangle = [\hat{U}_m(\Delta\tau)]^k |\Phi_{\text{rand}}\rangle, \quad (37)$$

$$\beta_k = \frac{k\Delta\tau}{1 - u_k/l}, \quad (38)$$

$$u_k = \frac{1}{N_s} \frac{\langle \Phi_{\text{rand}} | \hat{U}_m(\Delta\tau)^{2k} \hat{H} | \Phi_{\text{rand}} \rangle}{\langle \Phi_{\text{rand}} | \hat{U}_m(\Delta\tau)^{2k} | \Phi_{\text{rand}} \rangle}, \quad (39)$$

where  $l$  represents a constant. At first look, one might think that the mTPQ state is just a first-order cTPQ state ( $n_{\text{max}} = 1$ ). However, the definition of the inverse temperature is different. In the denominator of  $\beta_k$ ,  $u_k/l$  is introduced in the mTPQ state. This correction to  $\beta$  may

reduce the error caused by the finite-order expansion of  $\hat{U}(\Delta\tau)$ . From these definitions, it is obvious that the mTPQ states become equivalent to the cTPQ state by taking the large  $l$  limit, i.e., the small  $\Delta\tau$  limit.

In the TPQ calculation, we prepare several different initial wave functions ( $|\Phi_{\text{rand}}^n\rangle$ ,  $n = 0, 1, \dots, N-1$ ) and evaluate the average values and the errors originating from the choice of the initial states. In the procedure, we use the following bootstrap method:

1. Choosing  $P$  samples from  $N$  samples  $M$  times with replacement. We evaluate the average values of the physical quantities  $\hat{A}$  and the norm for each sample  $m$  as follows:

$$|\Phi^{\mathcal{R}_m(p)}(\beta_k)\rangle = \hat{U}(\Delta\tau)^k |\Phi_{\text{rand}}^{\mathcal{R}_m(p)}\rangle, \quad (40)$$

$$A_m(\beta_k) = \sum_{p=0}^{P-1} \langle \Phi^{\mathcal{R}_m(p)}(\beta_k) | \hat{A} | \Phi^{\mathcal{R}_m(p)}(\beta_k) \rangle, \quad (41)$$

$$Z_m(\beta_k) = \sum_{p=0}^{P-1} \langle \Phi^{\mathcal{R}_m(p)}(\beta_k) | \Phi^{\mathcal{R}_m(p)}(\beta_k) \rangle, \quad (42)$$

$$\langle A_m(\beta_k) \rangle = \frac{A_m(\beta_k)}{Z_m(\beta_k)}, \quad (43)$$

where  $\mathcal{R}_m(p)$  is a randomly chosen number in  $P$  samples and  $m$  represents the index of the bootstrap sampling ( $m = 0, 1, \dots, M-1$ ). We note that it is acceptable to duplicate each sample, i.e.,  $\mathcal{R}_m(p) = \mathcal{R}_m(q)$  for  $p \neq q$  is acceptable.

2. Then, we evaluate the average values and the error of the physical quantities as

$$\bar{A}(\beta_k) = \frac{1}{M} \sum_{m=0}^{M-1} \langle A_m(\beta_k) \rangle, \quad (44)$$

$$\sigma[A(\beta_k)]^2 = \frac{1}{M-1} \sum_{m=0}^{M-1} [A_m(\beta_k)^2 - \bar{A}(\beta_k)^2]. \quad (45)$$

In the cTPQ method,  $\beta_k$  is the same for each initial state. Thus, the bootstrap sampling can be done by the above procedure. In contrast, in the mTPQ method,  $\beta_k$  becomes different for each initial state although its difference is small in many cases. Therefore, we should do interpolation or extrapolation of the physical quantities to do the bootstrap sampling for the mTPQ states. However, this may make the error estimation for the mTPQ method complicated. Therefore, we recommend that users use the cTPQ method to be able to estimate the errors accurately. Nevertheless, the mTPQ method is still a useful and simple method for capturing general trends of target systems because the mTPQ requires only one matrix-vector operation.

Here, we explain the technical details of the TPQ calculations. Since  $Z_m(\beta_k)$  becomes exponentially large by lowering the temperature, it is necessary to normalize  $Z_m(\beta_k)$  with a proper factor. A simple way to conduct normalization is to use  $\mathcal{W}(\beta_k) = \langle \Phi^0(\beta_k) | \Phi^0(\beta_k) \rangle$ , i.e., the squared norm at the zeroth initial state. Under normalization, the physical quantities are given as

$$\tilde{Z}_m(\beta_k) = \frac{Z_m(\beta_k)}{\mathcal{W}(\beta_k)}, \quad \tilde{A}_m(\beta_k) = \frac{A_m(\beta_k)}{\mathcal{W}(\beta_k)}, \quad (46)$$

$$\langle A_m(\beta_k) \rangle = \frac{\tilde{A}_m(\beta_k)}{\tilde{Z}_m(\beta_k)}. \quad (47)$$

In the actual calculations, we obtain  $\tilde{A}_m(\beta_k)$  and  $\tilde{Z}_m(\beta_k)$ , then perform the bootstrap calculations. We note that the information of the norm is output in `Norm_n.dat` ( $n$  represents the number of the initial states) in  $\mathcal{H}\Phi$ . The squared norm of  $|\Psi(\beta_k)\rangle$  is defined as

$$N_k = \langle \Psi(\beta_k) | \Psi(\beta_k) \rangle. \quad (48)$$

In `Norm_m.dat`, the relative squared norm  $D_k$  is outputted since the value of  $N_k$  also becomes exponentially large. The definition of the relative norm  $D_k$  is

$$D_0 = N_0 = \langle \Phi_{\text{rand}} | \Phi_{\text{rand}} \rangle, \quad (49)$$

$$D_k = \frac{N_k}{N_{k-1}} \quad (\text{for } k > 0). \quad (50)$$

From the relative squared norm, we can calculate the norm as

$$N_k = \prod_{l=0}^k D_l. \quad (51)$$

### 3.5.2. Benchmark for the Heisenberg model

Here, we show a benchmarking result of the cTPQ method for the  $L$ -site one-dimensional Heisenberg model ( $L = 12, 16, 20, 24$ ). A sample script is available in Ref. [75]. We calculate several physical quantities, such as the specific heat  $C$ , the entropy  $S$ , and the magnetic susceptibility  $\chi$ , which are defined as

$$C = \frac{\langle \hat{H}^2 \rangle - \langle \hat{H} \rangle^2}{T^2}, \quad (52)$$

$$S = \frac{\log Z + \frac{\langle \hat{H} \rangle}{T}}{\log d_{\text{H}}}, \quad (53)$$

$$\chi_z = \frac{\langle \hat{S}_z^2 \rangle - \langle \hat{S}_z \rangle^2}{T} = \frac{\langle \hat{S}^2 \rangle - \langle \hat{S} \rangle^2}{3T}, \quad (54)$$

$$\hat{S}_z = \sum_i \hat{S}_{iz}, \quad (55)$$

$$\hat{S} = \sum_i (\hat{S}_{ix}, \hat{S}_{iy}, \hat{S}_{iz}), \quad (56)$$

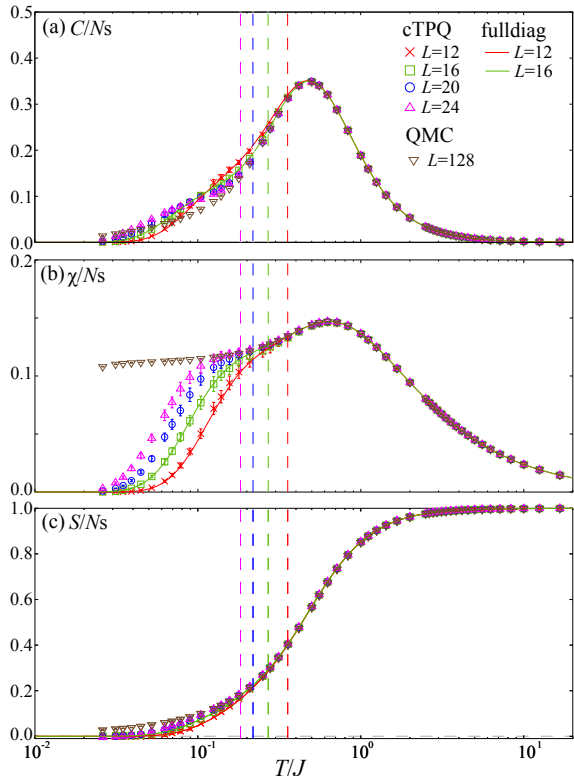


Figure 8: Temperature dependence of (a) specific heat  $C$ , (b) the uniform magnetic susceptibility  $\chi$ , and (c) the entropy  $S$ . The results of the cTPQ (full diagonalization) calculations are shown by symbols (lines). We note  $\chi$  is calculated from the fluctuation of total  $S_z$  ( $S$ ) in the cTPQ method (full diagonalization). We also show the results by the quantum Monte Carlo (QMC) method for large system size ( $L = 128$ ). The QMC calculation is done using DSQSS v2.0.4 [81, 82]. Error bars arising from Monte Carlo samplings are shown, but all of them are smaller than the symbol sizes. The vertical broken lines show the singlet-triplet gap for  $L = 12, 16$ , and  $20$ .

where  $d_H$  is the Hilbert dimensions of the given systems ( $d_H = 2^L$  for the one-dimensional Heisenberg model). In the cTPQ calculation, we take  $n_{\max} = 6$  and  $\Delta\tau = 0.02$ . In the bootstrap sampling, we take  $N$  independent initial states, and choose  $P$  samples  $M$  times from  $N$  samples with replacement. In this calculation, we take  $P = N = 200$ , and  $M = N/2 = 100$ .

As shown in Fig. 8, the cTPQ method well reproduces the results obtained by the full diagonalization for  $L = 12$  and  $L = 16$ . Although the total dimension is not so large for  $L = 12$  ( $d_H = 2^{12} = 4096$ ), the results of the cTPQ methods are consistent with those of the full diagonalization within the error. We note that the difference between physical quantities calculated by the cTPQ method and those by the canonical ensemble

becomes exponentially small as a function of the Hilbert dimension  $d_H$  [10]. We also compare the results by the quantum Monte Carlo (QMC) method for large system size ( $L = 128$ ) with those by the cTPQ method. Above the singlet-triplet gap arising from finite-size effects (shown by the broken lines), we find that the cTPQ method well reproduces the result by QMC, which can be regarded as the thermodynamic-limit values in the calculated temperature region. These results demonstrate that the cTPQ method is a reliable method for calculating the finite-temperature properties of quantum-many body systems.

## 4. Update of Standard mode

### 4.1. Important keywords

To simplify the input format in  $\mathcal{H}\Phi$ , we prepare Standard mode, which enables us to perform calculations for standard quantum lattice models. We first give an overview of the basic keywords used in Standard mode; `model`, `method`, and `lattice`. Here, we denote the keywords used in Standard mode by the typewriter font such as `model`. We list the available models, methods, and lattices in Table 1.

#### 4.1.1. Remarks on the keyword `model`

Below, we give several remarks on the models. Regarding spin models, we can treat general spin- $S$  Heisenberg models other than the  $S = 1/2$  one. For example, by specifying

```
2S=2
```

in Standard mode, one can treat the  $S = 1$  Heisenberg model. In Expert mode, by preparing the amplitude of spin at each site in `localspin.def`, it is possible to treat mixed spin systems, e.g., spin systems with  $S = 1/2$  and  $S = 1$  spins.

If one does not specify the total  $S_z$  in `model="Hubbard"`, one can treat the Hubbard-type model without total  $S_z$  conservation. Although `HubbardGC` allows us to treat the systems without particle-number conservation, the one-body and two-body terms that break the particle-number conservation (anomalous terms) are not implemented in either Standard mode or Expert mode of  $\mathcal{H}\Phi$ .

In Standard mode, we can treat the Kondo-lattice model, which consists of  $S = 1/2$  spins and itinerant electrons systems. In Expert mode, we can treat the general- $S$  Kondo-lattice model by changing `localspin.def` properly.

Table 1: Main keywords used in Standard mode of  $\mathcal{H}\Phi$ .

Model name	Explanation
Spin	Spin- $S$ Heisenberg model with total $S_z$ conservation
SpinGC	Spin- $S$ Heisenberg model <i>without</i> total $S_z$ conservation
SpinCMA	Continuous memory access method for SpinGC systems [83]
Hubbard	Hubbard model with particle $N$ conservation and with/without total $S_z$ conservation
HubbardGC	Hubbard model <i>without</i> particle $N$ conservation and total $S_z$ conservation
Kondo	Kondo lattice model with particle $N$ conservation and total $S_z$ conservation
KondoGC	Kondo lattice model <i>without</i> total $S_z$ and particle $N$ conservation
Method name	Explanation
FullDiag	Full diagonalization using LAPACK, ScaLAPACK, and MAGMA
Lanczos	Ground-state and spectrum calculations using the Lanczos method
CG	Ground-state (spectrum) calculations using the LOBPCG (shifted-Krylov) method
TPQ	mTPQ method for finite-temperature calculation
cTPQ	cTPQ method for finite-temperature calculation
Time-Evolution	Real-time evolution
Lattice name	Explanation
Chain	One-dimensional chain lattice
Ladder	$N$ -leg ladder
Square	Two-dimensional square lattice
Triangular	Two-dimensional triangular lattice
Honeycomb	Two-dimensional honeycomb structure
Kagome	Two-dimensional kagome lattice
Cubic	Three-dimensional monoatomic simple cubic lattice
FCO	Three-dimensional monoatomic face-centered orthorhombic lattice
Pyrochlore	Three-dimensional pyrochlore structure
Wannier90	Input from the transfer integrals and interactions in the Wannier90 format

#### 4.1.2. Remarks on the keyword method

We first note that `Lanczos` and `CG` are used both for ground-state calculations and spectrum calculations. In the spectrum calculations, `Lanczos` (`CG`) refers to the spectrum calculations by the continued-fraction expansion (shifted-Krylov method). `TPQ` means the micro-canonical TPQ method. However, as we mentioned above, the `cTPQ` method is recommended for the actual calculations since the procedure of the error estimation is straightforward.

#### 4.1.3. Remarks on the keyword lattice

In  $\mathcal{H}\Phi$ , several typical lattice structures are prepared for use in Standard mode. Keywords `L`, `W`, and `Height` represent the lengths of the system sites in the  $x$ ,  $y$ , and  $z$  directions, respectively. Unnecessary lengths in higher dimensions (e.g., `Height` in a two-dimensional lattice) can be omitted. Note that `H` is a keyword for a magnetic field. Standard mode can also treat more complicated lattice structures such as a tilted lattice. Here, we

give the specifications of the lattice structure in Standard mode: Let  $\mathbf{a}_0$ ,  $\mathbf{a}_1$ , and  $\mathbf{a}_2$  be unit vectors in real space. The position of the unit cell is described by

$$\mathbf{R} = r_0\mathbf{a}_0 + r_1\mathbf{a}_1 + r_2\mathbf{a}_2, \quad (57)$$

where  $r_i$  ( $i = 0, 1, 2$ ) is an integer. We consider the finite-size lattice (supercell) spanned by the linear combination of these unit vectors. The linear combination is defined as

$$\begin{pmatrix} \mathbf{A}_0 \\ \mathbf{A}_1 \\ \mathbf{A}_2 \end{pmatrix} = N \begin{pmatrix} \mathbf{a}_0 \\ \mathbf{a}_1 \\ \mathbf{a}_2 \end{pmatrix}, \quad (58)$$

$$N = \begin{pmatrix} N_{00} & N_{01} & N_{02} \\ N_{10} & N_{11} & N_{12} \\ N_{20} & N_{21} & N_{22} \end{pmatrix}, \quad (59)$$

where  $N_{ij}$  ( $i, j = 0, 1, 2$ ) is an integer.  $N_{i0}$ ,  $N_{i1}$ ,  $N_{i2}$  are specified by `aiW`, `aiL`, and `aiH` ( $i = 0, 1, 2$ ). Unit vectors and the Wyckoff positions for the two- and three-

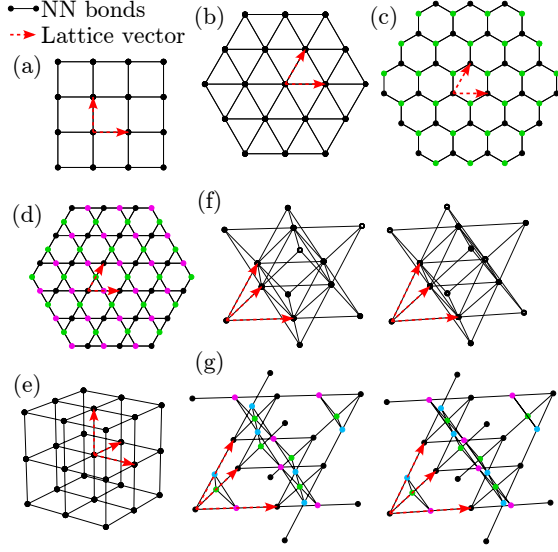


Figure 9: Two- and three-dimensional predefined lattices: (a) square lattice, (b) triangular lattice, (c) honeycomb lattice, (d) kagome lattice (e) simple cubic lattice, (f) face-centered cubic lattice, (g) pyrochlore structure. (f) and (g) are cross-eyed stereograms.

dimensional lattices defined in Standard mode are summarized below (see also Fig. 9):

- Square lattice [Fig. 9 (a)]

The unit lattice vectors are

$$\mathbf{a}_0 = (1, 0, 0), \quad (60)$$

$$\mathbf{a}_1 = (0, 1, 0). \quad (61)$$

- Triangular lattice, honeycomb lattice, kagome lattice [Figs. 9 (b, c, d)]

The unit lattice vectors are

$$\mathbf{a}_0 = (1, 0, 0), \quad (62)$$

$$\mathbf{a}_1 = \left( \frac{1}{2}, \frac{\sqrt{3}}{2}, 0 \right). \quad (63)$$

The honeycomb lattice has two sites in a unit cell,

$$\mathbf{0}, \quad \frac{\mathbf{a}_0}{3} + \frac{\mathbf{a}_1}{3}, \quad (64)$$

while the kagome lattice has the three sites

$$\mathbf{0}, \quad \frac{\mathbf{a}_0}{2}, \quad \frac{\mathbf{a}_1}{2}. \quad (65)$$

- Simple cubic lattice [Fig. 9 (e)]

The unit lattice vectors are

$$\mathbf{a}_0 = (1, 0, 0), \quad (66)$$

$$\mathbf{a}_1 = (0, 1, 0), \quad (67)$$

$$\mathbf{a}_2 = (0, 0, 1). \quad (68)$$

- Face-centered cubic lattice, pyrochlore structure [Figs. 9 (f, g)]

The unit lattice vectors are

$$\mathbf{a}_0 = \left( 0, \frac{1}{2}, \frac{1}{2} \right), \quad (69)$$

$$\mathbf{a}_1 = \left( \frac{1}{2}, 0, \frac{1}{2} \right), \quad (70)$$

$$\mathbf{a}_2 = \left( \frac{1}{2}, \frac{1}{2}, 0 \right). \quad (71)$$

The pyrochlore structure has the following four sites in a unit cell:

$$\mathbf{0}, \quad \frac{\mathbf{a}_0}{2}, \quad \frac{\mathbf{a}_1}{2}, \quad \frac{\mathbf{a}_2}{2}. \quad (72)$$

We also note that the wave numbers, which are compatible with the above real-space lattice, can be obtained as follows. The reciprocal vectors are defined as

$$\mathbf{b}_0 = 2\pi \frac{\mathbf{a}_1 \times \mathbf{a}_2}{\mathbf{a}_0 \cdot (\mathbf{a}_1 \times \mathbf{a}_2)}, \quad (73)$$

$$\mathbf{b}_1 = 2\pi \frac{\mathbf{a}_2 \times \mathbf{a}_0}{\mathbf{a}_1 \cdot (\mathbf{a}_2 \times \mathbf{a}_0)}, \quad (74)$$

$$\mathbf{b}_2 = 2\pi \frac{\mathbf{a}_0 \times \mathbf{a}_1}{\mathbf{a}_2 \cdot (\mathbf{a}_0 \times \mathbf{a}_1)}. \quad (75)$$

The position of the unit cell in the reciprocal space is defined as

$$\mathbf{K} = k_0 \mathbf{b}_0 + k_1 \mathbf{b}_1 + k_2 \mathbf{b}_2. \quad (76)$$

Since  $\mathbf{R}$  and  $\mathbf{R} + \mathbf{A}_i$  are equivalent, the following relation holds for the commensurate wave vector:

$$e^{i\mathbf{K}_{\text{com}} \cdot \mathbf{R}} = e^{i\mathbf{K}_{\text{com}} \cdot (\mathbf{R} + \mathbf{A}_i)} = 1. \quad (77)$$

In general, the commensurate wave vectors are given by

$$\mathbf{K}_{\text{com}} = m_0 \mathbf{B}_0 + m_1 \mathbf{B}_1 + m_2 \mathbf{B}_2, \quad (78)$$

$$(\mathbf{B}_0, \mathbf{B}_1, \mathbf{B}_2) = (\mathbf{b}_0, \mathbf{b}_1, \mathbf{b}_2) N^{-1}, \quad (79)$$

where  $m_i$  is an integer and  $N$  is the total number of unit cells.

## 5. Support for Wannier90 format

$\mathcal{H}\Phi$  supports reading input files of transfer integrals, direct-Coulomb and exchange integrals written in Wannier90 format [65, 66] by setting `mode="wannier90"`. Using this mode, the following Hamiltonian can be defined:

$$\mathcal{H} = \mathcal{H}_{1\text{body}} + \mathcal{H}_{2\text{body}} \quad (80)$$

$$\mathcal{H}_{1\text{body}} = \sum_{m,n,i,j,\sigma} t_{mn}(\mathbf{R}_{ij}) c_{im\sigma}^\dagger c_{jn\sigma} \quad (81)$$

$$\mathcal{H}_{2\text{body}} = \mathcal{H}_U + \mathcal{H}_J \quad (82)$$

$$\begin{aligned} \mathcal{H}_U &= \sum_{i,m} U_{mn}(\mathbf{0}) n_{im,\uparrow} n_{im,\downarrow} \\ &+ \sum_{(i,m)<(j,n)} U_{mn}(\mathbf{R}_{ij}) n_{im} n_{jn} \\ \mathcal{H}_J &= - \sum_{(i,m)<(j,n)} J_{mn}(\mathbf{R}_{ij}) (n_{im,\uparrow} n_{jn,\uparrow} + n_{im,\downarrow} n_{jn,\downarrow}) \\ &+ \sum_{(i,m)<(j,n)} J_{mn}(\mathbf{R}_{ij}) (c_{im,\uparrow}^\dagger c_{jn,\uparrow} c_{jn,\downarrow}^\dagger c_{im,\downarrow} + \text{h.c.}) \\ &+ \sum_{(i,m)<(j,n)} J_{mn}(\mathbf{R}_{ij}) (c_{im,\uparrow}^\dagger c_{jn,\uparrow} c_{im,\downarrow}^\dagger c_{jn,\downarrow} + \text{h.c.}), \quad (83) \end{aligned}$$

where  $\mathbf{R}_{ij} = \mathbf{R}_j - \mathbf{R}_i$ . Here,  $t_{mn}(\mathbf{R}_{ij})$ ,  $U_{mn}(\mathbf{R}_{ij})$ ,  $J_{mn}(\mathbf{R}_{ij})$  are a transfer integral, Coulomb and exchange integrals between  $m$ -orbit at  $\mathbf{R}_i$  and  $n$ -orbit at  $\mathbf{R}_j$ , and can be specified by the input files named as `zvo_hr.dat`, `zvo_ur.dat`, and `zvo_jr.dat` in the `dir-model` directory, respectively. These terms correspond to the on-site Coulomb interaction (`CoulombIntra`), the off-site Coulomb interaction (`CoulombInter`), the Hund couplings (`Hund`), the exchange couplings (`Exchange`), and the pairhopping terms (`Pairhopping`). Here, the geometry of the lattice can be defined by the input file named as `zvo_geom.dat`. Below, we detail the format of these files.

Information regarding the lattice structure is specified in `zvo_geom.dat` and is defined as follows:

```
a0x a0y a0z
a1x a1y a1z
a2x a2y a2z
Nwan
C0x C0y C0z
C1x C1y C1z
...
```

In the first three lines, the components of the unit vectors ( $\mathbf{a}_i$ ) are specified. The number of Wannier orbitals ( $N_{\text{wan}}$ ) is defined in the fourth line. After the fifth line, the center positions of the Wannier orbitals ( $\mathbf{C}_i$ ) are given in fractional coordinates.

The parameters of the Hamiltonians such as the transfer integrals (`zvo_hr.dat`), the Coulomb interactions (`zvo_ur.dat`), and the exchange interactions (`zvo_jr.dat`) can be specified in the Wannier90 format. We note that  $\mathcal{H}\Phi$  only supports the *reducible* representation, i.e., that each translation vector is regarded as independent. Below, we summarize the structure of the Wannier90 format with a reducible representation for transfer integrals.

```
Comment
Nwan
Nscel
1 ... 1
1 ... 1
Rx Ry Rz m n Re[tmn(R)] Im[tmn(R)]
```

In the Wannier90 format, the first line can be any text. The number of Wannier orbitals ( $N_{\text{wan}}$ ) is given in the second line, the number of supercells ( $N_{\text{scel}}$ ) is specified by the third line, the degeneracy of each Wigner-Seitz grid point is given in the fourth line<sup>3</sup>, and the information on the parameters of Hamiltonians is given in the following line. We note that the number of degeneracies should be arranged as 15 pieces in each line. The position vector is represented by  $\mathbf{R} = (R_x, R_y, R_z)$  and orbital indices are shown by  $m$  and  $n$ . Each line corresponds to the following transfer integrals  $t_{mn}(\mathbf{R}_{ij} = \mathbf{R} - \mathbf{0})$  [ $\mathbf{R}_i = \mathbf{0}$  and  $\mathbf{R}_j = \mathbf{R}$ ], defined in Eq. (81). Using the same format, direct Coulomb integrals  $U_{mn}(\mathbf{R})$  and direct exchange integrals  $J_{mn}(\mathbf{R})$  can be defined by `zvo_ur.dat` and `zvo_jr.dat`, respectively.

As a simple example, we show the input files for the two-dimensional Hubbard model with  $t = 1$ ,  $U = 4$  on a square lattice. The lattice geometry is given by `zvo_geom.dat`.

```
1.0000000000 0.0000000000 0.0000000000
0.0000000000 1.0000000000 0.0000000000
0.0000000000 0.0000000000 1.0000000000
1
0.5000000000 0.5000000000 0.5000000000
```

In this case, unit vectors are given by

$$\begin{aligned} \mathbf{a}_0 &= (1, 0, 0), \\ \mathbf{a}_1 &= (0, 1, 0), \\ \mathbf{a}_2 &= (0, 0, 1). \end{aligned}$$

<sup>3</sup>Since we do not use the information of the degeneracy in  $\mathcal{H}\Phi$ , we always set the degeneracy as 1 for simplicity.

In the fourth line, the number of Wannier orbitals ( $N_{\text{wan}}$ ) is outputted (in this case,  $N_{\text{wan}} = 1$ ). The center position of the Wannier orbital is defined as

$$\mathbf{C}_0 = 0.5\mathbf{a}_0 + 0.5\mathbf{a}_1 + 0.5\mathbf{a}_2. \quad (84)$$

Next, the nearest-neighbor transfer integrals are specified by `zvo_hr.dat` given as follows:

```
wannier90 format
  1
  9
  1  1  1  1  1  1  1  1  1
 -1 -1  0  1  1  0.0 0.0
 -1  0  0  1  1 -1.0 0.0
 -1  1  0  1  1  0.0 0.0
  0 -1  0  1  1 -1.0 0.0
  0  0  0  1  1  0.0 0.0
  0  1  0  1  1 -1.0 0.0
  1 -1  0  1  1  0.0 0.0
  1  0  0  1  1 -1.0 0.0
  1  1  0  1  1  0.0 0.0
```

Note that the transfer integral is defined by  $-t$  in  $\mathcal{H}\Phi$ . Thus, -1 in `zvo_hr.dat` means  $t = 1$ . Finally, the on-site Coulomb interactions are specified by `zvo_ur.dat` given as follows:

```
wannier90 format
  1
  9
  1  1  1  1  1  1  1  1  1
 -1 -1  0  1  1  0.0 0.0
 -1  0  0  1  1  0.0 0.0
 -1  1  0  1  1  0.0 0.0
  0 -1  0  1  1  0.0 0.0
  0  0  0  1  1  4.0 0.0
  0  1  0  1  1  0.0 0.0
  1 -1  0  1  1  0.0 0.0
  1  0  0  1  1  0.0 0.0
  1  1  0  1  1  0.0 0.0
```

The lattice size is specified using the input file of the standard mode of  $\mathcal{H}\Phi$ . Below, an example of the input file of the standard mode of  $\mathcal{H}\Phi$  is shown:

```
model = "Hubbard"
lattice = "Wannier90"
W = 2
L = 2
method = "CG"
2Sz = 0
nelec = 4
exct = 1
```

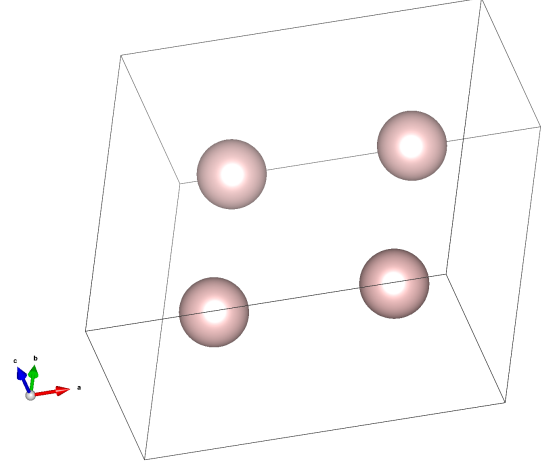


Figure 10: Visualization of the xsf file for a  $2 \times 2$  square lattice by VESTA [84].

In this case, the  $N_s = 2 \times 2$  lattice is defined. The lattice structure is output in the xsf format (`lattice.xsf`). One can confirm the lattice structure using visualization software such as VESTA [84]. In Fig. 10, we show the lattice structure visualized by VESTA.

## 6. Interface to RESPACK

$\mathcal{H}\Phi$  can make input files from the *ab initio* low-energy effective Hamiltonians derived by RESPACK, which are specified in the Wannier90 format. In this section, we give an overview of the derivation of the *ab initio* effective Hamiltonians and the format of output/input files.

### 6.1. Derivation of *ab initio* low-energy effective Hamiltonians

We explain how to derive the effective Hamiltonians from *ab initio* calculations. We first obtain the global band structures for the target compounds using the software packages for *ab initio* calculations such as Quantum ESPRESSO [85, 86] and xTAPP [87]. Then, we construct Wannier functions that describe the low-energy degrees of freedom of the target compounds. Finally, using the Wannier functions, we obtain the low-energy effective Hamiltonians defined in Eq. (80).

In RESPACK, the transfer integral  $t_{mn}(\mathbf{R}_{ij})$  is evaluated as

$$t_{mn}(\mathbf{R}_{ij}) = \int_V d\mathbf{r} d\mathbf{r}' w_{m0}^*(\mathbf{r}) H_0(\mathbf{r}, \mathbf{r}') w_{n\mathbf{R}}(\mathbf{r}'). \quad (85)$$



Table 2: Main output files by RESPACK. We assume the prefix of the file name is zvo. Note that  $\mathcal{H}\Phi$  and mVMC support the Wannier90 format with the reducible representation.

File name	Explanation
zvo_geom.dat	Information of the lattice unit vectors and positions of the Wannier centers
zvo_hr.dat	Transfer integrals $t_{mn}(\mathbf{R}_{ij})$ (Wannier90 format)
zvo_ur.dat	Coulomb interactions $U_{mn}(\mathbf{R}_{ij})$ (Wannier90 format)
zvo_jr.dat	Exchange interactions $J_{mn}(\mathbf{R}_{ij})$ (Wannier90 format)
zvo_dr.dat	Expectation values by Kohn-Sham Hamiltonians $D_{mn}(\mathbf{R}_{ij})$ (Wannier90 format)

Here,  $V$  is the volume of the crystal,  $w_{i\mathbf{R}}(\mathbf{r})$  is the  $i$ th Wannier function at the  $\mathbf{R}$ th cell, and  $H_0(\mathbf{r}, \mathbf{r}')$  is the Kohn-Sham Hamiltonian. The static screened direct integrals  $U_{mn}(\mathbf{R})$  and the static screened exchanged integrals  $J_{mn}(\mathbf{R})$  are given as follows:

$$\begin{aligned}
 U_{mn}(\mathbf{R}) &= \int_V d\mathbf{r}d\mathbf{r}' w_{m\mathbf{0}}^*(\mathbf{r})w_{n\mathbf{0}}(\mathbf{r})W(\mathbf{r}, \mathbf{r}')w_{n\mathbf{R}}^*(\mathbf{r}')w_{m\mathbf{R}}(\mathbf{r}'), \\
 J_{mn}(\mathbf{R}) &= \int_V d\mathbf{r}d\mathbf{r}' w_{m\mathbf{0}}^*(\mathbf{r})w_{n\mathbf{R}}(\mathbf{r})W(\mathbf{r}, \mathbf{r}')w_{n\mathbf{R}}^*(\mathbf{r}')w_{m\mathbf{0}}(\mathbf{r}').
 \end{aligned}$$

Here,  $W(\mathbf{r}, \mathbf{r}')$  is the screened Coulomb interactions. The information on lattice geometry, the positions of the Wannier centers, and the expectation values of the Kohn-Sham Hamiltonian are also outputted. We summarize the output files by RESPACK in Table 2. The parameters of the Hamiltonian and one-body expectation values are output in `zvo_hr.dat`, `zvo_ur.dat`, `zvo_jr.dat` and `zvo_dr.dat`, respectively.

We note that the following elimination of the double counting of the chemical potential is necessary for multi-orbital systems [88, 89]:

$$\mathcal{H} = \sum_{m,i,\sigma} [t_{mm}(0) - t_{mm}^{\text{DC}}(0)] c_{im\sigma}^\dagger c_{im\sigma}, \quad (86)$$

where  $t_{mm}^{\text{DC}}(0)$  is the one-body correction term given as:

$$\begin{aligned}
 t_{mm}^{\text{DC}}(\mathbf{0}) &= \alpha U_{mm}(\mathbf{0})D_{mm}(\mathbf{0}) \\
 &+ \sum_{(\mathbf{R},n) \neq (\mathbf{0},m)} U_{mn}(\mathbf{R})D_{nm}(\mathbf{0}) \\
 &- (1 - \alpha) \sum_{(\mathbf{R},n) \neq (\mathbf{0},0)} J_{mn}(\mathbf{R})D_{nm}(\mathbf{R}), \quad (87)
 \end{aligned}$$

$$D_{mn}(\mathbf{R}_{ij}) = \sum_{\sigma} \langle c_{im\sigma}^\dagger c_{jn\sigma} \rangle_{\text{KS}}, \quad (88)$$

where  $\alpha$  specifies how to treat the effects of the on-site Coulomb interactions and the exchange couplings. In the standard calculation, we take  $\alpha = 1/2$ . Information regarding  $D_{mn}(\mathbf{R}_{ij})$  is outputted in `zvo_dr.dat`.

Corrections to the one-body terms other than the chemical potentials can be defined as follows:

$$\begin{aligned}
 t_{mn}^{\text{DC}}(\mathbf{R}_{ij}) &= \frac{1}{2} J_{mn}(\mathbf{R}_{ij})(D_{nm}(\mathbf{R}_{ji}) \\
 &+ 2\text{Re}[D_{nm}(\mathbf{R}_{ji})]) - \frac{1}{2} U_{mn}(\mathbf{R}_{ij})D_{nm}(\mathbf{R}_{ji}) \\
 &(\mathbf{R}_{ij}, m) \neq (\mathbf{0}, n). \quad (89)
 \end{aligned}$$

However, these corrections originate from the Fock terms, and they are not fully included in the *ab initio* calculations. Moreover, these corrections may greatly change the band structures in strong coupling regions. Therefore, we recommend not introducing these off-site corrections in the actual calculations. Nevertheless,  $\mathcal{H}\Phi$  can include these Fock-type corrections by a keyword `Fock` because it may be necessary for examining the effects of the off-site corrections.

## 6.2. Calculation by $\mathcal{H}\Phi$

An example of an input file used with Standard mode of  $\mathcal{H}\Phi$  is shown as follows.

```

model = "Hubbard"
lattice = "Wannier90"
cutoff_length_t = 1
cutoff_length_u = 1
cutoff_length_j = 1
W = 2
L = 2
Height = 1
method = "CG"
2Sz = 0
nelec = 4
exct = 1

```

By using `lattice="Wannier90"`,  $\mathcal{H}\Phi$  reads the information of the effective Hamiltonians and generates the input files. Since the tractable systems sizes by  $\mathcal{H}\Phi$  is not large, it is often necessary to omit the long-range hoppings and interactions, whose length is larger than half of the linear dimensions of the system sizes. To cut off the long-range part of the Hamiltonian, `cutoff_length_t`, `cutoff_length_u`, and

cutoff\_length\_j are used. If one wants to omit the small parameters in the Hamiltonians, one can specify the lower limit of the absolute values of the parameters by cutoff\_t, cutoff\_u, and cutoff\_j. For example, if  $|t_{mn}(\mathbf{R}_{ij})| < \text{cutoff\_t}$ , those hopping parameters are ignored. A tutorial on the derivation and the analysis of the low-energy effective Hamiltonian for  $\text{Sr}_2\text{CuO}_3$  can be found on the web page of  $\mathcal{H}\Phi$  [62].

## 7. Summary and Discussion

To summarize, we first explained the installation of the current version of  $\mathcal{H}\Phi$  in Sec. 2. We also mentioned the submodule repository of Standard mode. We also explained newly added functions/methods, such as full diagonalization using GPGPU and ScaLAPACK in Sec. 3.1, spectral calculations using the shifted Krylov method in Sec. 3.2, the locally optimal block preconditioned conjugate gradient (LOBPCG) method for obtaining several eigenvectors at once in Sec. 3.3, real-time evolution in Sec. 3.4, and the canonical TPQ (cTPQ) method in Sec. 3.5. In Sec. 4, we explain the updates to Standard mode such as the newly added keywords for methods (e.g., CG for the LOBPCG method and cTPQ for the cTPQ method) and lattice structures (e.g. FCO for the face-centered orthorhombic lattice and Wannier90 for the Wannier90 format). In Sec. 5, we explained how to specify Hamiltonians in the Wannier90 format.  $\mathcal{H}\Phi$  can perform the calculations for the *ab initio* low-energy effective Hamiltonians obtained by RESPACK, which outputs the information in the Wannier90 format, as we explained in Sec. 6.

Here, we mention recently developed packages for exact diagonalization, such as QuSpin [90–92] and QS<sup>3</sup>[93, 94]. QuSpin is an open-source Python package for exact diagonalization, which can treat spin, fermionic, and bosonic systems. Besides ground-state calculations, quantum dynamics such as quench dynamics can also be performed using QuSpin. QS<sup>3</sup> is a software package that focuses on performing exact diagonalization near fully polarized states for the spin-1/2 XXZ Heisenberg model. Since the Hilbert dimension near fully polarized states is small, it is possible to have huge system sizes. For example, it is shown that the exact diagonalization for a system size of  $10^3 = 10 \times 10 \times 10$  with three down spins (the Hilbert dimension is about  $1.6 \times 10^9$ ) is possible using QS<sup>3</sup>. QS<sup>3</sup> also supports calculations of dynamical spin structure factors. Compared to these software packages, the main advantage of  $\mathcal{H}\Phi$  is supporting massively parallel computation. As we already showed in the previous paper [19], the parallelization efficiency from 4096 cores to 32,768

cores reaches about 80%. Thus, using massively parallel supercomputers,  $\mathcal{H}\Phi$  can perform not only ground-state calculations, but also finite-temperature calculations, excited-state calculations, and real-time evolution for a wide range of quantum lattice models. Since each software package has its own advantage, the complementary use of several different packages is useful for efficiently completing research.

Lastly, we mention future extensions of  $\mathcal{H}\Phi$ . One is the implementation of the reduction of dimensions of the Hilbert space by using translational symmetry and point-group symmetry. It is shown that the reduction of the dimensions enables us to perform exact diagonalization calculations for up to 50 sites in spin-1/2 systems [95]. To reduce the finite-size effects, which is the main disadvantage of the exact diagonalization method, the implementation of reduction by symmetry is useful. Recently, an efficient algorithm [96] (trie-based ranking) is proposed for finding bit patterns that satisfy a given condition. Combination of the reduction of the Hilbert space and the recently proposed efficient bit ranking algorithm can enable us to perform the state-of-the-art exact diagonalization using  $\mathcal{H}\Phi$ . Another intriguing function is the finite-temperature spectrum calculations. It is shown that the shifted Krylov method enables us to perform exact finite-temperature spectrum calculations [97]. Implementing finite-temperature spectrum calculations is desirable for direct comparison with the experimental spectrum obtained at finite temperatures. These further extensions will make  $\mathcal{H}\Phi$  a more useful software package and will be reported in the near future.

## Acknowledgement

We wish to thank Takeo Hoshi, Tomohiro Sogabe, and Kazuma Nakamura for fruitful discussions. We also wish to thank users of  $\mathcal{H}\Phi$  for their feedback and helpful contributions. TM thanks Tsuyoshi Okubo for useful discussions on the cTPQ method. A part of the calculations was done using the Supercomputer Center, the Institute for Solid State Physics, the University of Tokyo. KI, YM, KY, and TM were supported by Building of Consortia for the Development of Human Resources in Science and Technology, MEXT, Japan. This study was also supported by Grants-in-Aid for Scientific Research Nos. 19H01809, 20H00122, 20H01850, 23H01092, and 23H03818 from the Ministry of Education, Culture, Sports, Science and Technology, Japan. This work was also supported by the National Natural Science Foundation of China (Grant No. 12150610462). The development of  $\mathcal{H}\Phi$  was supported by ‘‘Project for advance-

ment of software usability in materials science” [98] in the fiscal year 2015, 2016, 2017, and 2018. The implementation of the full diagonalization using GPGPU was supported by the “support service of program portability to General Purpose Graphics Processing Unit,” which was operated by the Institute for Solid State Physics in the fiscal year 2017.

## References

- [1] E. Dagotto, [Correlated electrons in high-temperature superconductors](#), *Rev. Mod. Phys.* 66 (1994) 763–840.
- [2] [Frustrated Spin Systems](#), ed. H. Diep (World Scientific, Singapore, 2005).
- [3] L. Balents, [Spin liquids in frustrated magnets](#), *Nature* 464 (7286) (2010) 199–208.
- [4] Y. Motome, J. Nasu, [Hunting Majorana Fermions in Kitaev Magnets](#), *J. Phys. Soc. Jpn.* 89 (1) (2020) 012002.
- [5] E. Anderson, Z. Bai, C. Bischof, L. Blackford, J. Demmel, J. Dongarra, J. Du Croz, A. Greenbaum, S. Hammarling, A. McKenney, D. Sorensen, [LAPACK Users’ Guide](#), 3rd Edition, Society for Industrial and Applied Mathematics, 1999.
- [6] L. S. Blackford, J. Choi, A. Cleary, E. D’Azevedo, J. Demmel, I. Dhillon, J. Dongarra, S. Hammarling, G. Henry, A. Petitet, K. Stanley, D. Walker, R. C. Whaley, [ScaLAPACK Users’ Guide](#), Society for Industrial and Applied Mathematics, Philadelphia, PA, 1997.
- [7] M. Imada, M. Takahashi, [Quantum Transfer Monte Carlo Method for Finite Temperature Properties and Quantum Molecular Dynamics Method for Dynamical Correlation Functions](#), *J. Phys. Soc. Jpn.* 55 (10) (1986) 3354–3361.
- [8] A. Hams, H. De Raedt, [Fast algorithm for finding the eigenvalue distribution of very large matrices](#), *Phys. Rev. E* 62 (2000) 4365–4377.
- [9] S. Sugiura, A. Shimizu, [Thermal Pure Quantum States at Finite Temperature](#), *Phys. Rev. Lett.* 108 (2012) 240401.
- [10] S. Sugiura, A. Shimizu, [Canonical Thermal Pure Quantum State](#), *Phys. Rev. Lett.* 111 (2013) 010401.
- [11] S. Lloyd, [Pure state quantum statistical mechanics and black holes](#), arXiv:1307.0378.
- [12] F. Jin, D. Willsch, M. Willsch, H. Lagemann, K. Michielsen, H. De Raedt, [Random State Technology](#), *J. Phys. Soc. Jpn.* 90 (1) (2021) 012001.
- [13] [http://www.stat.phys.titech.ac.jp/~nishimori/titpack2\\_new/index-e.html](http://www.stat.phys.titech.ac.jp/~nishimori/titpack2_new/index-e.html).
- [14] [http://quattro.phys.sci.kobe-u.ac.jp/Kobe\\_Pack/Kobe\\_Pack.html](http://quattro.phys.sci.kobe-u.ac.jp/Kobe_Pack/Kobe_Pack.html).
- [15] <http://www-e.uni-magdeburg.de/jschulen/spin/>.
- [16] F. Alet, P. Dayal, A. Grzesik, A. Honecker, M. Körner, A. Läuchli, S. R. Manmana, I. P. McCulloch, F. Michel, R. M. Noack, et al., [The ALPS project: open source software for strongly correlated systems](#), *J. Phys. Soc. Jpn.* 74 (Suppl) (2005) 30–35.
- [17] A. F. Albuquerque, F. Alet, P. Corboz, P. Dayal, A. Feiguin, S. Fuchs, L. Gamper, E. Gull, S. Gürtler, A. Honecker, et al., [The ALPS project release 1.3: Open-source software for strongly correlated systems](#), *Journal of Magnetism and Magnetic Materials* 310 (2) (2007) 1187–1193.
- [18] B. Bauer, L. Carr, H. G. Evertz, A. Feiguin, J. Freire, S. Fuchs, L. Gamper, J. Gukelberger, E. Gull, S. Guertler, et al., [The ALPS project release 2.0: open source software for strongly correlated systems](#), *J. Stat. Mech.: Theory Exp.* 2011 (05) (2011) P05001.
- [19] M. Kawamura, K. Yoshimi, T. Misawa, Y. Yamaji, S. Todo, N. Kawashima, [Quantum lattice model solver HQ](#), *Comput. Phys. Commun.* 217 (2017) 180–192.
- [20] <https://www.pasums.iissp.u-tokyo.ac.jp/hphi/en/>.
- [21] T. Misawa, Y. Yamaji, [Finite-Temperature Signatures of Spin Liquids in Frustrated Hubbard Model](#), *J. Phys. Soc. Jpn.* 87 (2) (2018) 023707.
- [22] A. M. Samarakoon, G. Wachtel, Y. Yamaji, D. A. Tennant, C. D. Batista, Y. B. Kim, [Classical and quantum spin dynamics of the honeycomb  \$\Gamma\$  model](#), *Phys. Rev. B* 98 (2018) 045121.
- [23] A. Catuneanu, Y. Yamaji, G. Wachtel, Y. B. Kim, H.-Y. Kee, [Path to stable quantum spin liquids in spin-orbit coupled correlated materials](#), *npj Quantum Mater.* 3 (1) (2018) 23.
- [24] K. Ido, T. Misawa, [Correlation effects on the magnetization process of the Kitaev model](#), *Phys. Rev. B* 101 (2020) 045121.
- [25] T. Misawa, Y. Motoyama, Y. Yamaji, [Asymmetric melting of a one-third plateau in kagome quantum antiferromagnets](#), *Phys. Rev. B* 102 (2020) 094419.
- [26] C. Xu, J. Feng, M. Kawamura, Y. Yamaji, Y. Nahas, S. Prokhorenko, Y. Qi, H. Xiang, L. Bellaiche, [Possible Kitaev Quantum Spin Liquid State in 2D Materials with  \$S = 3/2\$](#) , *Phys. Rev. Lett.* 124 (2020) 087205.
- [27] A. S. Patri, M. Hosoi, Y. B. Kim, [Distinguishing dipolar and octupolar quantum spin ices using contrasting magnetostriction signatures](#), *Phys. Rev. Res.* 2 (2020) 023253.
- [28] A. S. Patri, M. Hosoi, S. Lee, Y. B. Kim, [Theory of magnetostriction for multipolar quantum spin ice in pyrochlore materials](#), *Phys. Rev. Res.* 2 (2020) 033015.
- [29] T. Yamada, T. Suzuki, S.-i. Suga, [Ground-state properties of the  \$K - \Gamma\$  model on a honeycomb lattice](#), *Phys. Rev. B* 102 (2020) 024415.
- [30] K. Yoshimi, T. Tsumuraya, T. Misawa, [Ab initio derivation and exact diagonalization analysis of low-energy effective Hamiltonians for  \$\beta - X\[\text{Pd}\(\text{dmit}\)\_2\]\_2\$](#) , *Phys. Rev. Res.* 3 (2021) 043224.
- [31] J. Yoshitake, J. Nasu, Y. Kato, Y. Motome, [Majorana-magnon crossover by a magnetic field in the Kitaev model: Continuous-time quantum Monte Carlo study](#), *Phys. Rev. B* 101 (2020) 100408.
- [32] T. Misawa, K. Yoshimi, T. Tsumuraya, [Electronic correlation and geometrical frustration in molecular solids: A systematic ab initio study of  \$\beta - X\[\text{Pd}\(\text{dmit}\)\_2\]\_2\$](#) , *Phys. Rev. Res.* 2 (2020) 032072.
- [33] S.-H. Jang, R. Sano, Y. Kato, Y. Motome, [Computational design of  \$f\$ -electron Kitaev magnets: Honeycomb and hyperhoneycomb compounds  \$A\_2\text{PrO}\_3\$  \( \$A = \text{alkali metals}\$ \)](#), *Phys. Rev. Mater.* 4 (2020) 104420.
- [34] P. Laurell, S. Okamoto, [Dynamical and thermal magnetic properties of the Kitaev spin liquid candidate  \$\alpha\$ - \$\text{RuCl}\_3\$](#) , *npj Quantum Mater.* 5 (1) (2020) 2.
- [35] S.-H. Jang, Y. Kato, Y. Motome, [Vortex creation and control in the Kitaev spin liquid by local bond modulations](#), *Phys. Rev. B* 104 (2021) 085142.
- [36] Y. Nomura, M. Imada, [Dirac-Type Nodal Spin Liquid Revealed by Refined Quantum Many-Body Solver Using Neural-Network Wave Function, Correlation Ratio, and Level Spectroscopy](#), *Phys. Rev. X* 11 (2021) 031034.
- [37] G. Sala, M. B. Stone, B. K. Rai, A. F. May, P. Laurell, V. O. Garlea, N. P. Butch, M. D. Lumsden, G. Ehlers, G. Pokharel, et al., [Van Hove singularity in the magnon spectrum of the antiferromagnetic quantum honeycomb lattice](#), *Nat. Commun.* 12 (1) (2021) 171.
- [38] X.-P. Yao, R. L. Luo, G. Chen, [Intertwining  \$SU\(N\)\$  symmetry and frustration on a honeycomb lattice](#), *Phys. Rev. B* 105 (2022) 024401.
- [39] M. Hosoi, E. Z. Zhang, A. S. Patri, Y. B. Kim, [Uncovering](#)

- Footprints of Dipolar-Octupolar Quantum Spin Ice from Neutron Scattering Signatures, *Phys. Rev. Lett.* 129 (2022) 097202.
- [40] A. M. Samarakoon, P. Laurell, C. Balz, A. Banerjee, P. Lampen-Kelley, D. Mandrus, S. E. Nagler, S. Okamoto, D. A. Tennant, Extraction of interaction parameters for  $\alpha$ - $\text{RuCl}_3$  from neutron data using machine learning, *Phys. Rev. Res.* 4 (2022) L022061.
- [41] A. Rayyan, D. Churchill, H.-Y. Kee, Field-induced Kitaev multipolar liquid in spin-orbit coupled  $d^2$  honeycomb Mott insulators, *Phys. Rev. B* 107 (2023) L020408.
- [42] H. Zhang, L. Jin, S. Wang, B. Xi, X. Shi, F. Ye, J.-W. Mei, Effective Hamiltonian for nickelate oxides  $\text{Nd}_{1-x}\text{Sr}_x\text{NiO}_2$ , *Phys. Rev. Res.* 2 (2020) 013214.
- [43] D. Betto, R. Fumagalli, L. Martinelli, M. Rossi, R. Piombo, K. Yoshimi, D. Di Castro, E. Di Gennaro, A. Sambri, D. Bonn, G. A. Sawatzky, L. Braicovich, N. B. Brookes, J. Lorenzana, G. Ghiringhelli, Multiple-magnon excitations shape the spin spectrum of cuprate parent compounds, *Phys. Rev. B* 103 (2021) L140409.
- [44] A. Iwano, Y. Yamaji, Superconductivity in Bilayer  $t$ - $t'$  Hubbard Models, *J. Phys. Soc. Jpn.* 91 (9) (2022) 094702.
- [45] H. Araki, T. Mizoguchi, Y. Hatsugai,  $\mathbb{Z}_2$  Berry phase for higher-order symmetry-protected topological phases, *Phys. Rev. Res.* 2 (2020) 012009.
- [46] A. A. Markov, A. N. Rubtsov, Local marker for interacting topological insulators, *Phys. Rev. B* 104 (2021) L081105.
- [47] K. Ido, M. Imada, T. Misawa, Charge dynamics of correlated electrons: Variational description with inclusion of composite fermions, *Phys. Rev. B* 101 (2020) 075124.
- [48] M. Charlebois, M. Imada, Single-Particle Spectral Function Formulated and Calculated by Variational Monte Carlo Method with Application to  $d$ -Wave Superconducting State, *Phys. Rev. X* 10 (2020) 041023.
- [49] R. Martinazzo, E. Pollak, Lower bounds to eigenvalues of the Schrödinger equation by solution of a 90-y challenge, *Proc. Natl. Acad. Sci. U.S.A.* 117 (28) (2020) 16181–16186.
- [50] M. Ronto, E. Pollak, R. Martinazzo, Comparison of an improved self-consistent lower bound theory with Lehmann’s method for low-lying eigenvalues, *Sci. Rep.* 11 (1) (2021) 23450.
- [51] Y. Nomura, Helping restricted Boltzmann machines with quantum-state representation by restoring symmetry, *J. Condens. Matter Phys.* 33 (17) (2021) 174003.
- [52] Y. Nomura, N. Yoshioka, F. Nori, Purifying Deep Boltzmann Machines for Thermal Quantum States, *Phys. Rev. Lett.* 127 (2021) 060601.
- [53] K. Inui, Y. Kato, Y. Motome, Determinant-free fermionic wave function using feed-forward neural networks, *Phys. Rev. Res.* 3 (2021) 043126.
- [54] W. Dobraz, V. M. Katukuri, N. A. Bogdanov, D. Kats, G. Li Manni, A. Alavi, Combined unitary and symmetric group approach applied to low-dimensional Heisenberg spin systems, *Phys. Rev. B* 105 (2022) 195123.
- [55] T. Hoshi, M. Kawamura, K. Yoshimi, Y. Motoyama, T. Misawa, Y. Yamaji, S. Todo, N. Kawashima, T. Sogabe,  $K\omega$ -Open-source library for the shifted Krylov subspace method of the form  $(zI - H)x = b$ , *Comput. Phys. Commun.* 258 (2021) 107536.
- [56] A. Frommer, BiCGStab( $\ell$ ) for Families of Shifted Linear Systems, *Computing* 70 (2) (2003) 87–109.
- [57] A. V. Knyazev, Toward the optimal preconditioned eigensolver: Locally optimal block preconditioned conjugate gradient method, *SIAM journal on scientific computing* 23 (2) (2001) 517–541.
- [58] <http://icl.cs.utk.edu/magma/software>.
- [59] K. Nakamura, Y. Yoshimoto, Y. Nomura, T. Tadano, M. Kawamura, T. Kosugi, K. Yoshimi, T. Misawa, Y. Motoyama, RESPACK: An ab initio tool for derivation of effective low-energy model of material, *Comput. Phys. Commun.* 261 (2021) 107781.
- [60] <https://sites.google.com/view/kazuma7k6r>.
- [61] <https://www.pasums.issp.u-tokyo.ac.jp/hphi/en/doc/manual/>.
- [62] <http://issp-center-dev.github.io/HPhi/manual/master/en/html/wannier/tutorial.html>.
- [63] S. Yamamoto, T. Sogabe, T. Hoshi, S.-L. Zhang, T. Fujiwara, Shifted Conjugate-Orthogonal-Conjugate-Gradient Method and Its Application to Double Orbital Extended Hubbard Model, *J. Phys. Soc. Jpn.* 77 (11) (2008) 114713.
- [64] S. Yamada, T. Imamura, M. Machida, Preconditioned conjugate gradient method for large-scale eigenvalue problem of quantum problem: Convergence property of adaptive-shift preconditioner, *Transactions of JSCES* 2006 (27) (2006) 20060027.
- [65] <http://www.wannier.org>.
- [66] G. Pizzi, V. Vitale, R. Arita, S. Blügel, F. Freimuth, G. Géranton, M. Gibertini, D. Gresch, C. Johnson, T. Koretsune, et al., Wannier90 as a community code: new features and applications, *J. Condens. Matter Phys.* 32 (16) (2020) 165902.
- [67] <https://github.com/issp-center-dev/HPhi/releases>.
- [68] <https://cmake.org>.
- [69] <https://icl.utk.edu/projectsfiles/magma/doxygen/installing.html>.
- [70] T. Misawa, S. Morita, K. Yoshimi, M. Kawamura, Y. Motoyama, K. Ido, T. Ohgoe, M. Imada, T. Kato, mVMC-Open-source software for many-variable variational Monte Carlo method, *Comput. Phys. Commun.* 235 (2019) 447–462.
- [71] <https://github.com/issp-center-dev/mVMC>.
- [72] D. Tahara, M. Imada, Variational Monte Carlo Method Combined with Quantum-Number Projection and Multi-Variable Optimization, *J. Phys. Soc. Jpn.* 77 (11) (2008) 114701.
- [73] <https://math.nist.gov/MatrixMarket/>.
- [74] E. R. Gagliano, C. A. Balseiro, Dynamical Properties of Quantum Many-Body Systems at Zero Temperature, *Phys. Rev. Lett.* 59 (1987) 2999–3002.
- [75] <https://isspns-gitlab.issp.u-tokyo.ac.jp/hphi-dev/hphi-paper2023>.
- [76] J. des Cloizeaux, J. J. Pearson, Spin-Wave Spectrum of the Antiferromagnetic Linear Chain, *Phys. Rev.* 128 (1962) 2131–2135.
- [77] M. Sugihara, K. Murota, Theoretical Numerical Linear Algebra (Iwanami Studies in Advanced Mathematics).
- [78] [https://en.wikipedia.org/wiki/Gershgorin\\_circle\\_theorem](https://en.wikipedia.org/wiki/Gershgorin_circle_theorem).
- [79] M. Eckstein, M. Kollar, P. Werner, Thermalization after an Interaction Quench in the Hubbard Model, *Phys. Rev. Lett.* 103 (2009) 056403.
- [80] N. Tsuji, P. Barmettler, H. Aoki, P. Werner, Nonequilibrium dynamical cluster theory, *Phys. Rev. B* 90 (2014) 075117.
- [81] <https://github.com/issp-center-dev/dsqs>.
- [82] Y. Motoyama, K. Yoshimi, A. Masaki-Kato, T. Kato, N. Kawashima, DSQSS: Discrete Space Quantum Systems Solver, *Comput. Phys. Commun.* 264 (2021) 107944.
- [83] We note that SpinCMA only supports the limited lattice geometry. For details, please refer the manual.
- [84] K. Momma, F. Izumi, VESTA 3 for three-dimensional visualization of crystal, volumetric and morphology data, *J. Appl. Crystallogr.* 44 (6) (2011) 1272–1276.
- [85] P. Giannozzi, O. Andreussi, T. Brumme, O. Bunau, M. B. Nardelli, M. Calandra, R. Car, C. Cavazzoni, D. Ceresoli, M. Cococcioni, et al., Advanced capabilities for materials modelling with Quantum ESPRESSO, *J. of Phys.: Cond. Matt.* 29 (46) (2017) 465901.

- [86] <https://www.quantum-espresso.org>.
- [87] <http://xtapp.cp.is.s.u-tokyo.ac.jp>.
- [88] T. Misawa, K. Nakamura, M. Imada, **Magnetic Properties of Ab initio Model of Iron-Based Superconductors LaFeAsO**, J. Phys. Soc. Jpn. 80 (2) (2011) 023704.
- [89] H. Seo, S. Ishibashi, Y. Otsuka, H. Fukuyama, K. Terakura, **Electronic States of Single-Component Molecular Conductors [M(tmdt)<sub>2</sub>]**, J. Phys. Soc. Jpn. 82 (5) (2013) 054711.
- [90] <http://weinbe58.github.io/QuSpin/index.html>.
- [91] P. Weinberg, M. Bukov, **QuSpin: a Python Package for Dynamics and Exact Diagonalisation of Quantum Many Body Systems part I: spin chains**, SciPost Phys. 2 (2017) 003.
- [92] P. Weinberg, M. Bukov, **QuSpin: a Python Package for Dynamics and Exact Diagonalisation of Quantum Many Body Systems. Part II: bosons, fermions and higher spins**, SciPost Phys. 7 (2019) 20.
- [93] <https://github.com/QS-Cube/ED>.
- [94] H. Ueda, S. Yunoki, T. Shimokawa, **Quantum spin solver near saturation: QS<sup>3</sup>**, Comput. Phys. Commun. 277 (2022) 108369.
- [95] A. Wietek, A. M. Läuchli, **Sublattice coding algorithm and distributed memory parallelization for large-scale exact diagonalizations of quantum many-body systems**, Phys. Rev. E 98 (2018) 033309.
- [96] M. Wallerberger, K. Held, **Trie-based ranking of quantum many-body states**, arXiv:2203.04158.
- [97] Y. Yamaji, T. Suzuki, M. Kawamura, **Numerical Algorithm for Exact Finite Temperature Spectra and Its Application to Frustrated Quantum Spin Systems**, arXiv preprint arXiv:1802.02854 (2018).
- [98] <https://www.pasums.issp.u-tokyo.ac.jp/en>.